frontiers | Frontiers in Materials

TYPE Original Research
PUBLISHED 11 December 2024
DOI 10.3389/fmats.2024.1509403



OPEN ACCESS

EDITED BY
Alfonso Pedone,
University of Modena and Reggio Emilia, Italy

REVIEWED BY
Rajan Saini,
Rutgers, The State University of New Jersey, United States
Gigliola Lusvardi,
University of Modena and Reggio Emilia, Italy

*CORRESPONDENCE
Paivo Kinnunen,
paivo.kinnunen@oulu.fi

RECEIVED 10 October 2024
ACCEPTED 21 November 2024
PUBLISHED 11 December 2024

CITATION
Jiang C, Santos HS, Yliniemi J, Lindén J, Ramteke DD, Illikainen M, Cheeseman C and Kinnunen P (2024) Fe-bearing magnesium silicate glasses for potential supplementary cementitious applications.
*Front. Mater.* 11:1509403.
doi: 10.3389/fmats.2024.1509403



# Fe-bearing magnesium silicate glasses for potential supplementary cementitious applications

Chuqing Jiang[1], Hellen Silva Santos[1], Juho Yliniemi[1], Johan Lindén[2], D. D. Ramteke[1], Mirja Illikainen[1], Christopher Cheeseman[3] and Paivo Kinnunen[1]*

[1]Fibre and Particle Engineering Research Unit, University of Oulu, Oulu, Finland, [2]Physics, Faculty of Natural Sciences and Technology, Åbo Akademi University, Turku, Finland, [3]Department of Civil and Environmental Engineering, Imperial College London, London, United Kingdom

Supplementary cementitious materials (SCMs) are used to minimize $CO_2$ emissions associated with cement production. However, their global supply is insufficient to meet the growing market demand for cement and concrete, being essential to develop alternative SCMs based on abundant waste streams and low-cost resources. Fe-bearing Mg-based glasses are promising candidates with the potential to utilize high-volume feedstocks rich in Fe and Mg, but their effectiveness relies on deep understanding of the relationship between glass composition, reactivity, and pozzolanic properties. In this study, Fe-Mg silicate glasses with varying Fe concentrations were precisely engineered through a sol-gel route to better understand the impact of Fe on the glass structure and reactivity. While $Fe^{3+}$ typically acts as a glass network former, it was observed to also function as an intermediate cation, behaving either as a network former or modifier. Glass reactivity was assessed through aqueous dissolution tests, revealing that the composition and chemical environment of $Fe^{3+}$ within the glass network significantly influence the dissolution behavior. The introduction of Fe into Mg-Si glasses increased overall reactivity, potentially due to Fe-induced phase separation and the increasing of [$FeO_6$] octahedra sites at higher Fe concentrations, which was also associated to network depolymerization. These findings deepen the understanding of the role of $Fe^{3+}$ in magnesium silicate glasses, provide key insights into optimizing glass reactivity by fine-tuning the composition, and indicate the potential of these glasses as promising SCMs.

KEYWORDS

**sustainability, sol-gel, glass, reactivity, phase separation, magnesium silicate glasses, supplementary cementitious materials (SCMs)**

## 1 Introduction

Portland cement production accounts for ~8% of the global anthropogenic $CO_2$ emissions annually (Scrivener et al., 2018). To mitigate these emissions supplementary cementitious materials (SCMs), such as silica fume, coal fly ash, and ground granulated blast furnace slag, have been employed as partial replacements of Portland cement (Juenger and Siddique, 2015; Serdar et al., 2019), aligned with the main actions in CEMBUREAU's net zero roadmap by 2050 (CEMBUREAU, 2020). However, the limited availability of these

materials presents challenges in meeting the growing demand for cement (Serdar et al., 2019). Since the reactivity of SCMs is primarily driven by their glassy or amorphous phases (Skibsted and Snellings, 2019a), the development of synthetic glasses with tunable properties has emerged as a promising alternative (Micoulaut et al., 2015; Mascaraque et al., 2017). Synthetic glasses offer the advantage of precisely controlling chemical composition, particle size, and surface properties, making possible to fine-tune their reactivity and pozzolanic behavior to meet the specific needs of cementitious systems.

Traditionally, glasses are synthesized through the melt-quenching technique, which requires high temperatures (above 1,400°C), leading to high energy consumption and associated $CO_2$ emissions (Mackenzie, 1982; Fiume et al., 2020). In contrast, the sol-gel process offers a low-energy, potentially eco-friendly alternative, operating at significantly lower temperatures (400°C and 700°C) while producing highly pure and homogeneous materials with controllable properties (Wenzel, 1985; Dislich, 1986; Baccile et al., 2009; Foroutan et al., 2015). Sol-gel methods are employed in several industrial fields that require accurate control over glass properties (e.g., optics, biomedicine and sensor industries) (Zheng and Boccaccini, 2017; Aminirastabi et al., 2018; B; Figueira et al., 2021). Former works have reported the use of glass materials as supplementary cementitious materials (Li et al., 2019; Skibsted and Snellings, 2019b; Alzeer et al., 2022a), however, a better understanding of the relation between the glass composition and reactivity is still needed to allow further technological developments in the field. The sol-gel technique has been used in studies of cementitious materials to enhance the calcium silicate hydrate (C-S-H) structure by incorporating organic groups into the glass structure, and optimizing hydration mechanics, leading to improved physical properties and durability of hardened cement structures (Minet et al., 2006; Zarzuela et al., 2020; Nair et al., 2021). Thus, the sol-gel technique offers higher accuracy and control over synthetic variables, enabling a fine tuning of the composition and morphology of the produced glasses. For this reason, the current work opted for producing the synthetic glasses via a sol-gel method, aiming at producing glasses with targeted elemental compositions, and investigating the impact of the glass structure on their physico-chemical properties, as well as probing the potential of the glasses for applications as SCMs.

The chemical composition of synthetic glasses plays a crucial role in determining their properties, such as reactivity, thermal stability and mechanical properties (Yoldas, 1982; Kuryaeva, 2004). Glass reactivity depends largely on the degree of polymerization within the network, a key factor influencing its stability and dissolution behavior (Snellings, 2013). In turn, the degree of polymerization is primarily determined by the ratio of network modifiers to network formers (Schöler et al., 2017) Additional factors, such as phase separation, microstructural characteristics (e.g., density, porosity, specific surface area), and environmental conditions (e.g., temperature, pH), also influence reactivity (Kinnunen et al., 2019; Perez et al., 2019; Hamdan et al., 2023). Calcium-based glasses have been widely studied for SCM applications due to the ability of $Ca^{2+}$ to depolymerize glass networks (Diamond, 1983). However, the production of Ca-based glasses often involves the calcination of $CaCO_3$ to obtain CaO, with inherent $CO_2$ emissions, thereby limiting the sustainability of these materials (Lisa et al., 2006). Magnesium has similar chemical properties to Ca but offers more sustainable alternatives due to its possible near-zero-carbon feedstocks, such as Mg silicates and brine (Weisinger and Bellorín-Font, 1998). In our previous study, the addition of MgO significantly enhanced the reactivity of synthetic silicate glasses (Jiang et al., 2023). On a practical application, a higher Mg substitution for Ca in calcium aluminosilicate glasses has shown increased SCM reaction activity in glass-cement blends (Nie et al., 2020).

Iron, the fourth most abundant element in the Earth's crust, is commonly found in Mg-rich minerals such as olivine and pyroxene (Kim and Lee, 2019). Natural raw materials for alternative cements, such as clays and volcanic sources, often contain significant amounts of iron (Peys et al., 2022). These Fe-bearing Mg-Si minerals are known to have long-term geochemical stability, and their incorporation in cementitious systems is expected to enhance pozzolanic reactions, suggesting that Fe can improve the performance of SCMs in cementitious systems (Gartner and Myers, 1993). This understanding of the role of Fe in natural minerals supports the strategic use of synthetic glasses for cement applications. Studies further show that synthetic glasses offer superior reactivity, consistent quality and strong cementitious performance without the need for additional chemical activators or admixtures, offering advantages over natural mineral resources (Alzeer et al., 2022a; 2022b; Snellings et al., 2023). Thus, incorporating Fe into synthetic glasses designed for cement applications presents a forward-looking and environmentally responsible approach.

Glass networks are formed of strong covalent bonds between $[SiO_4]$ tetrahedra connected by bridging oxygens (BO) (Durdziński et al., 2015). Alkali and alkali earth (e.g., $Ca^{2+}$, $Na^{+}$, $Mg^{2+}$) ions can integrate into networks as modifiers, generating non-bridging oxygens (NBO) and remaining weakly bonded. Current understanding suggests that high-field strength cations (e.g., $Al^{3+}$, $Sc^{3+}$, $La^{3+}$) may play an "intermediate" role in glass structures, sharing some characteristics of network formers and network modifiers (Kelsey et al., 2009). It is reasonable to expect $Fe^{3+}$ to have the properties of an intermediate similar to $Al^{3+}$ because of their comparable ionic field strengths (56.6 $Å^{-2}$ for $Al^{3+}$ and 54.5 $Å^{-2}$ for $Fe^{3+}$) (Holland et al., 1999). Thus, although $Fe^{3+}$ typically acts as a network former, it has been found to also act as an intermediate cation, depending on its coordination environment (Holland et al., 1999; Pinakidou et al., 2008). $Fe^{3+}$ is often found in two different coordination environments within silicate glasses, particularly in alkaline and alkaline earth silicate glasses, forming both tetrahedra and octahedra units depending on the glass composition (Farges et al., 2004; Coey, 1974). It is suggested that at low concentrations, $Fe^{3+}$ primarily forms $[FeO_4]$ tetrahedra, contributing to the net structure as a network former, while a greater proportion of $[FeO_4]$ tetrahedra convert to $[FeO_6]$ octahedra as a network modifier when the iron concentration is increased (Baowei et al., 2013a; 2015). This versatility allows $Fe^{3+}$ to modify the glass network significantly, potentially enhancing key properties such as reactivity and mechanical strength.

This study investigates $Fe^{3+}$-bearing magnesium silicate glasses synthesized via sol-gel processing, aiming at assessing the impact of $Fe^{3+}$ on the structure and reactivity of Mg-Si glass systems. Our results showed that the concentration of $Fe^{3+}$ determines

TABLE 1 Sample codes for Fe-Mg-Si glasses with variable $X_{Fe}$ [nominal molar ratio of Fe/(Fe + Mg)], and the experimental chemical compositions determined by XRF measurements.

| Sample codes | Fe/(Fe + mg) (mol%) | | Mg/(Mg + Si) (mol%) | |
|---|---|---|---|---|
| | $X_{Fe}$ | XRF analysis | Nominal ratio | XRF analysis |
| G00 | 0 | — | 25 | 23.72 |
| G05 | 5 | 6.67 | 25 | 22.85 |
| G10 | 10 | 12.25 | 25 | 23.08 |
| G15 | 15 | 16.55 | 25 | 23.82 |
| G25 | 25 | 26.13 | 25 | 23.79 |
| G30 | 30 | 33.43 | 25 | 22.74 |
| G35 | 35 | 34.41 | 25 | 22.31 |
| G40 | 40 | 39.32 | 25 | 23.07 |
| G45 | 45 | 44.23 | 25 | 23.82 |
| G50 | 50 | 50.14 | 25 | 23.03 |
| G55 | 55 | 52.77 | 25 | 23.36 |

its role as network modifier and former in the glasses structure, impacting the reactivity of the produced glasses. While this work focuses on an initial evaluation of the reactivity through dissolution behavior, it offers valuable insights into the role of Fe in enhancing the performance of magnesium silicate glasses as a potential low-carbon SCM for future cement applications. It is expected that follow up research can be built from the results presented in the current work to develop suitable routes for utilizing Fe,Mg-rich feedstocks, such as inorganic waste streams, to produce SCMs with similar performance to the observed for synthetic glasses (Shanks et al., 2024). This approach holds potential not only to improve material performance but also to support sustainability by reducing dependence on raw materials and enabling the repurposing of industrial waste.

# 2 Experimental

## 2.1 Glass synthesis

Fe-bearing magnesium silicate glasses with different Fe contents [$(Mg_{1-X}Fe_X)SiO_3$ with $X_{Fe}$ = Fe/(Fe + Mg) from 0 to 55 mol%] and constant Mg/Si ratio [Mg/(Mg + Si) = 25 mol%] were prepared via a modified rapid sol-gel method. Sample codes are shown in Table 1, and their chemical compositions, expressed as oxide percentages, are provided in Table 2. The Mg/Si ratio was selected based on the previous study (Jiang et al., 2023), where binary magnesium silicate glasses with a Mg/(Mg + Si) ratio of 25 mol% showed the highest reactivity. Tetraethyl orthosilicate (TEOS, purity≥98%, Fisher Scientific, Germany) was employed as the precursor to establish the silica framework. Nitric acid ($HNO_3$, 65%, Merck, Germany) was used as a catalyst, with a concentration of 1 M

TABLE 2 Oxide composition of samples based on XRF analysis (in mol%).

| Sample codes | $Fe_2O_3$ (mol%) | MgO (mol%) | $SiO_2$ (mol%) |
|---|---|---|---|
| G00 | — | 23.72 | 76.28 |
| G05 | 0.81 | 22.66 | 76.53 |
| G10 | 1.58 | 22.71 | 75.71 |
| G15 | 2.31 | 23.27 | 74.42 |
| G25 | 4.04 | 22.83 | 73.13 |
| G30 | 5.40 | 21.52 | 73.08 |
| G35 | 5.53 | 21.08 | 73.39 |
| G40 | 6.96 | 21.47 | 71.57 |
| G45 | 8.63 | 21.76 | 69.61 |
| G50 | 10.38 | 20.64 | 68.98 |

in the solution. Magnesium nitrate hexahydrate [$Mg(NO_3)_2{\cdot}6H_2O$, 98.0%–102.0%, VWR BDH, Belgium] and iron (III) nitrate nonahydrate [$Fe(NO_3)_3{\cdot}9H_2O$, purity≥98%, VWR Alfa Aesar, United States] were utilized as the precursor for MgO and $Fe_2O_3$, respectively.

The sol-gel process is shown in Figure 1, adapted from reported Fe-containing sol-gel routes and modified to suit our system (Coroiu et al., 2005; Shankhwar and Srinivasan, 2016; Baino et al., 2018). TEOS was mixed with ethanol absolute (purity≥ 99.8%)

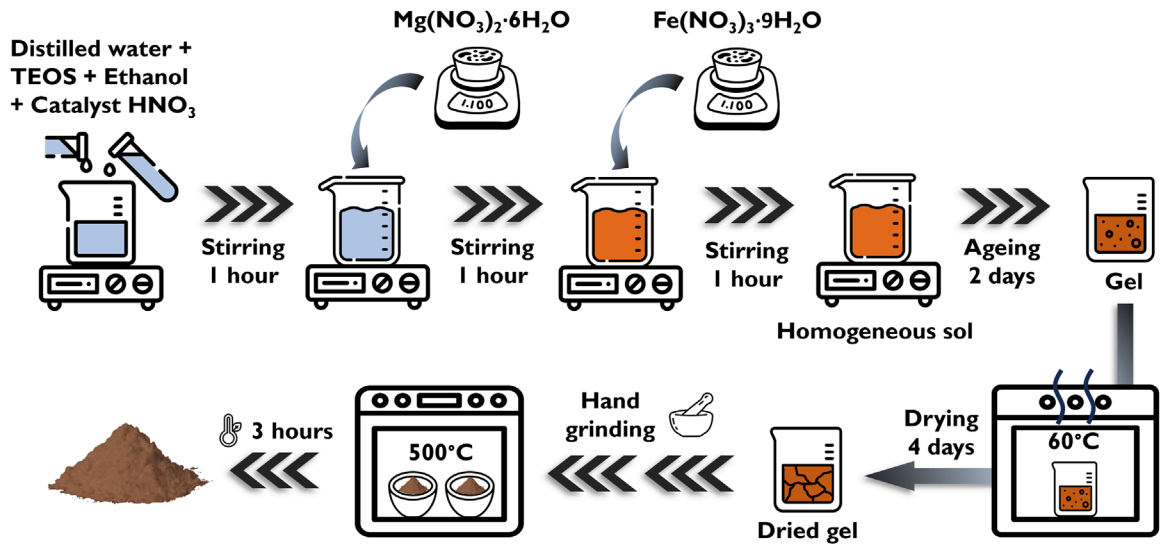


FIGURE 1
Procedure flow chart for the sol-gel route.

and deionized water at a molar ratio of EtOH: $H_2O$: TEOS = 4:4:1, while subjected to consistent stirring at 450 rpm at room temperature (22°C ± 1°C). $HNO_3$ was then added until the initial pH of the solution reached 1. One hour later, $Mg(NO_3)_2{\cdot}6H_2O$ and $Fe(NO_3)_3{\cdot}9H_2O$ were sequentially added into the system at 1-h intervals. The sol gradually turned from orange to brown, depending on Fe content. The sol was held at room temperature until a homogeneous wet gel formed. This ageing process took between 2 and 5 days. Wet gels underwent drying at 60°C for a duration of 4 days, yielding dried gels with a fluffy appearance, which are pulverized into powders by hand grinding. Finally, obtained powders were heated to 500°C for 3 h in the high-temperature furnace at a heating rate of 5°C/min.

## 2.2 Characterization

Thermogravimetric analysis (TGA) and differential scanning calorimetry (DSC) of dried gels were completed (SDT 650, TA Instruments, US). Glass powders weighing 15 mg were loaded into Pt crucibles and subjected to heating, ramping from 40°C to 1,010°C at a rate of 10 °C/min in a $N_2$ environment. The device was calibrated according to the ASTM E1582 standard, following the recommendations of the manufacturer. The equipment has a temperature precision of ±0.5°C, a calorimetric precision and accuracy of ±2%, a heat capacity accuracy of ±5%, a weighing accuracy of ±0.5%, and a weighing precision of ±0.1%.

X-ray diffraction (XRD) measurement was performed utilizing a Rigaku X-ray diffractometer (SmartLab 9 kW, Japan) running at 40 kV and 135 mA, equipped with Co K-beta radiation (λ = 1.620750 Å). At a scanning speed of 4°/min, diffraction patterns were obtained within the 2θ range of 10°–100°. Crystalline phases were identified using PDXL software (2nd version). A PANalytical X-ray fluorescence (XRF) spectrometer (Axios max 4 kW, Netherlands) was used to ascertain the chemical composition. The LECO CS230 analyzer (United States) was used to determine the residual carbon and sulfur concentration in glasses.

Scanning electron microscopy (ZEISS, Sigma HD VP, Oberkochen, Germany) was used to perform the morphologic characterization of glasses at an acceleration voltage of 5 kV. Before imaging, the samples underwent platinum sputter coating to form conductive layers. Elemental analysis was performed using an energy-dispersive X-ray spectroscopy (EDS) detector (Oxford, model Ultim Max 65) and the mapping analysis used Oxford Aztec software. STEM imaging was conducted using JEOL (JEM-2200FS) microscopy, coupled with the EDS detector (JEOL Dry SD100GV, 100 $mm^2$, 0.98 Sr). The specific surface areas were determined based on mass using the BET (Barrett-Emmett-Teller) model. Measurements were performed through $N_2$ physisorption at 300°C using a Micrometrics instrument (ASAP 2000). Laser diffraction particle size analysis was employed to acquire particle size distribution (PSD) data (Beckman Coulter LS 13320, Brea, CA, United States).

Data regarding the infrared active groups within glasses were acquired (Bruker, Vertex 80v, United States) using diffuse reflectance infrared Fourier transform (DRIFT) spectrometer in transmission mode. All measurements were completed at room temperature. For each sample, 40 scans spanning from 4,000 to 400 $cm^{-1}$ at a resolution of 4 $cm^{-1}$ were collected with baseline correction and normalization applied. X-ray photoelectron spectroscopy (XPS) was conducted with a Thermo Fisher Scientific instrument (model ESCALAB 250Xi, United Kingdom), using an X-ray source of Al (Kα = 1,486.6 eV) with a spot size of 650 μm and a CAE analyzer mode. The high-resolution elemental spectra were measured with a pass energy of 20 eV and an energy step size of 0.1 eV. The XPS data were analyzed utilizing Thermo Avantage software (v 5.9925, built 06702, Thermo Fisher Scientific).

To investigate the local structures of $Fe^{3+}$ in samples, Mössbauer measurements were conducted in transmission geometry using a 25 mCi Co-57(Rh) source from Rietverc Co, aged 10 months,

at room temperature. A linear Doppler velocity range with a maximum of 10.0 mm/s was apllied. Sample powders were thoroughly mixed with epoxy resin and placed in thin-walled, 3D-printed plastic containers with an inner diameter of 20 mm. The amount of sample varied according to the Fe concentration: 200 mg for G05, 130 mg for G25, and 75 mg for G45, ensuring sufficient absorption of the 14.4 keV gamma quanta used in the experiments. The spectra were fitted using a custom non-linear least-square fitting program, which incorporated the full Hamiltonian of combined electric and magnetic interactions. Fit parameters included the quadrupole-coupling constant ($eQVzz$), the isomer shift ($\delta$), component intensities ($I$), and internal field ($B_{eff}$) as applicable. The experimental line width ($\Gamma$) was constrained to match that of the non-magnetic components, while magnetic sextets were fitted with a separate line width parameter.

## 2.3 Dissolution test

The reactivity of glasses was evaluated based on the elemental solubility in water, with samples tested in duplicate. The dissolution test offers a straightforward and effective method for understanding the ability of glasses to release reactive species, which are crucial for pozzolanic or hydraulic reactions and are key to assessing their cementitious potential (Oey et al., 2020). Experiments were performed at room temperature (22°C ± 1°C). Before use, Milli-Q water underwent bubbling with $N_2$ (99.997%) to ensure the absence of dissolved $CO_2$. The experimental setup consisted of 300 mL polypropylene vessels with 0.01 g of glass powder dissolved in 100 g of solution (L/S = 10000). 0.05 wt% TIPA (tri-isopropanolamine, $C_9H_{21}NO_3$) was applied additively in solutions. Dissolution experiments were carried out on an IKA KS 260 orbital horizontal shaking table with continuous shaking at a speed of 250 rpm. Solutions were shaken continuously for 2 days. A 2 μm filter paper was used to filter the remaining solutions, which were then acidified to pH~2 with 2% $HNO_3$ and stored at 4°C. Aqueous concentrations of Fe, Mg and Si in filtered solutions were detected by inductively coupled plasma optical emission spectrometry (ICP-OES, Thermo Scientific, Model iCAP 6500 Duo).

# 3 Results and discussion

## 3.1 Optimization of preparation conditions

TG-DTG analysis was performed to determine the optimal heating temperature for the gels. Figure 2 presents the TGA and DTGA results for four dried gels with varying Fe contents. Three stages of mass loss are shown by the TG curves in Figure 2A. The first step occurs in the range 60°C–200°C, being attributed to the desorption of physically adsorbed water, and loss of residual water and ethanol (Montazerian et al., 2015). The decomposition of residual organic precursors can be associated with the second steep mass loss at around 250°C (Catauro et al., 2016; Ren et al., 2017). The third mass loss ranging from 300°C to 500°C relates to the removal of nitrate ions derived from the acidic catalyst and metal precursors (Saravanapavan and Hench, 2003). Figure 2B indicates that changes in weight become smaller and steady after the temperature reaches 500°C. The LECO test of G00 and G30 glasses reveals residual C and S contents below 0.5% and 0.01%, respectively. This suggests the absence of organic residues in samples (Supplementary Material S1). Based on TG and DTG results, heat treatment of gels at 500°C would allow minimizing the impurities in produced glasses.

The amorphous structure of the synthetic glasses heated at 500°C for 3 h was confirmed with XRD analyses of the G00 to G55 glasses (Figure 3). It can be observed from Figure 3A that glasses with $X_{Fe}$ less than 55% only have a broad reflection from 20° to 40° (2θ), which is the fingerprint of an amorphous structure. Some distinct reflections are seen in the G55 pattern, where the reflections correspond to the crystalline phase hematite (PDF#04-006-8177) defined in Figure 3B. When $X_{Fe}$ reaches 35%, some small reflections emerge, and appears in greater intensity with increasing Fe content. This can be attributed to the phase separation occurring in glasses. During heat treatment, $Mg_2(SiO_4)$ (Mg-rich), Si-rich and Fe-rich phases form through a nucleation process (Kinnunen et al., 2019; Enju et al., 2022). This phenomenon may result from minor variations and statistical fluctuations in thermal conditions during experiments. Despite these minor reflections, the matrix remains predominantly vitreous, as indicated by broad reflections in the XRD spectra. The faint, hard-to-identify reflections further suggest that G35 glass largely retains its glassy nature. XRD analysis demonstrates that the vitreous structures of synthetic Fe-bearing Mg-Si glasses are obtained when the $X_{Fe}$ is lower than 55%. Therefore, only glasses with $X_{Fe}$ below this threshold were included for further characterization and research. Combined with previous studies where Mg-Si glasses with Mg/(Mg + Si) less than 55% are amorphous (Jiang et al., 2023), the compositions of pure amorphous glasses fall within the narrow range shown in Supplementary Material S2.

## 3.2 Morphologic characterization

The surface morphologic features of G00 to G55 glasses are shown in Figure 4. The Fe content has no obvious effect on the glass morphology. SEM images indicate that all glasses have a large range of particle size distributions consisting of micron-sized clusters. Glass particles on the sub-micron scale are prone to agglomeration, forming larger clusters. Pores with the size of ~3 μm are observed in the G55 glass, while other samples show much smoother surfaces on large particles. SEM-EDS mapping reveals a generally uniform distribution of elements at the micrometer scale (Supplementary Material S3).

The particle size distribution (PSD) of 5 samples with different Fe contents is present in Figure 5A, where all glasses show a particle size ranging from 0 to 500 μm with a median size of ~100 μm. G00 shows the narrowest differential volume distribution curve with the smallest median size of about 66 μm (Supplementary Material S4). When Fe is introduced, the differential PSD curves broaden, which indicates that Fe doping deteriorates the homogeneity of glass particle sizes to some extent. Specific surface area (SSA) analysis of G00 to G50 glasses in Figure 5B shows that glasses with $X_{Fe}$ ranging from 0% to 40% have similar SSAs, while the G45 glass exhibits a relatively lower SSA and G50 a relatively higher one. Given that SSA influences glass dissolution, it will be considered when evaluating glass reactivity in this study. The correlation

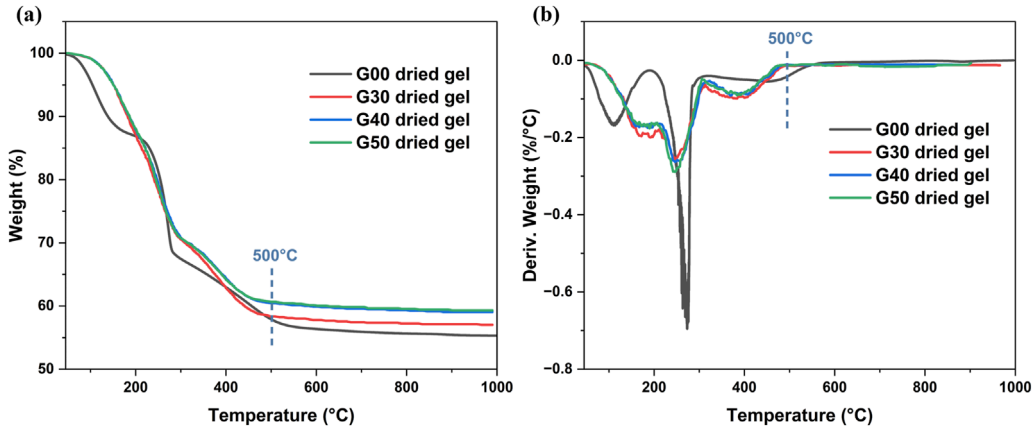


FIGURE 2
**(A)** Thermogravimetric analysis (TGA) and **(B)** corresponding differential TGA (DTGA) data of G00, G30, G40 and G50 dried gels. Weight changes become negligible above 500°C.

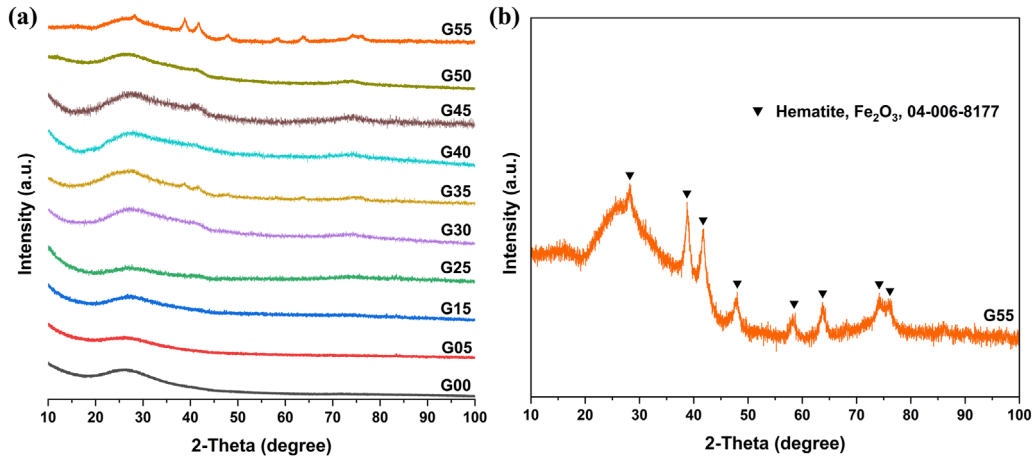


FIGURE 3
**(A)** XRD patterns of G00 to G55 glasses, and **(B)** indexed peaks of crystalline phases in G55. The amorphous structure is obtained when $X_{Fe}$ is lower than 55%. The crystalline $Fe_2O_3$ phase is detected in the G55 sample. Measurements were taken at 40 kV and 135 mA using Co K-beta radiation (λ = 1.62 Å).

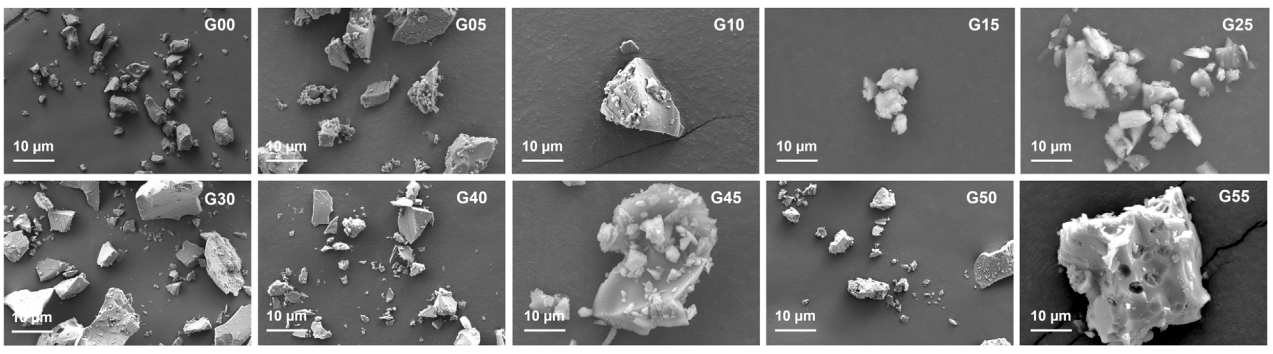


FIGURE 4
SEM images of G00 to G55 glasses. It can be observed that Fe content has no obvious effect on the glass morphology and glass particles are prone to agglomerate to form larger clusters. The G55 sample shows a different porous surface compared to other samples.

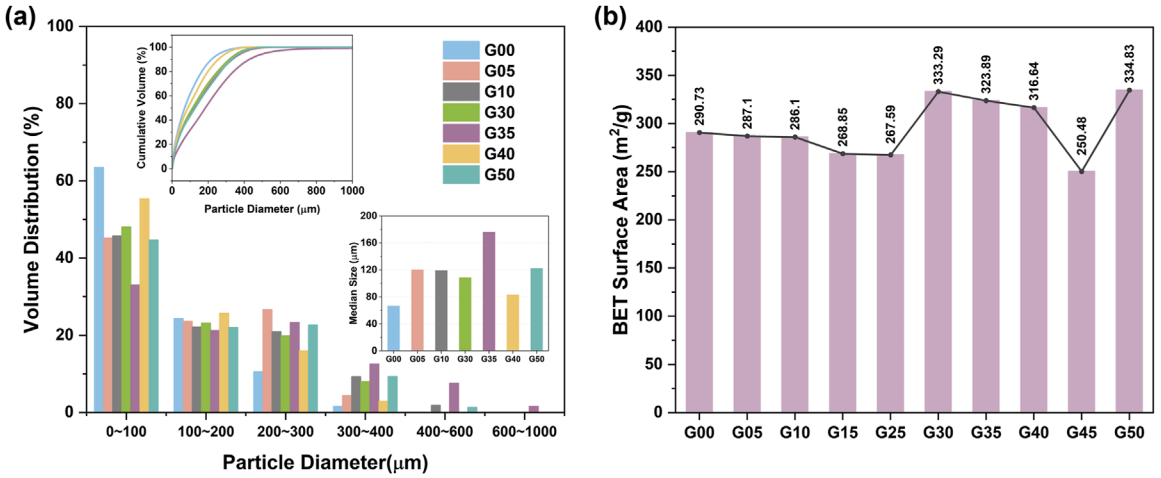


FIGURE 5
**(A)** Particle size distribution data and **(B)** specific surface area (SSA) measured via the BET method of glass with different Fe contents.

coefficient values from BET SSA analysis and PSD analysis are provided in Supplementary Material S4.

## 3.3 Evaluation of glass reactivity

The reactivity of the glasses was evaluated through dissolution testing. However, the supersaturation of Fe-hydroxides in water makes it difficult to accurately measure Fe solubility. To address this, TIPA was used as a chelating agent to mitigate Fe precipitation by forming ferric-alkanolamine complexes (Gartner and Myers, 1993; Peys et al., 2022). TIPA is commonly used as an additive in Portland cement to accelerate dissolution and hydration (Deng et al., 2022). In this study, 0.05 wt% TIPA was introduced into the solutions, with a control group tested without TIPA for comparison. Ionic concentrations measured by ICP-OES confirmed that TIPA effectively prevented Fe precipitation without affecting the dissolution of Mg and Si (Supplementary Material S5).

Glass reactivity is quantified as normalized mass loss ($Q_i$), defined as the mass of the target element $i$ released per unit area of glass (mg/m$^2$). $Q_i$ is calculated using the following equation (Equation 1) (Corkhill et al., 2013; Cheng et al., 2017):

$$Q_i = (C_i \cdot V_{sol})/(SSA \cdot m \cdot x_i) \quad (1)$$

where $C_i$ is the concentration of element $i$ in the solution (mol/L) determined by ICP measurements, $V_{sol}$ is the solution volume (L), SSA denotes the specific surface area of the glass (m$^2$/g), $m$ is the mass of glass used (g), and $x_i$ represents the mass fraction of element $i$ in the initial glass before the dissolution experiment.

Figure 6 presents the normalized mass loss results for Fe, Mg and Si of all glasses, along with the total normalized elemental mass loss. The data indicates that Fe-doped glasses exhibit higher overall reactivity compared to binary Mg-Si glasses. As shown in Figures 6A, B, the reactivity of the glasses, based on the dissolution of Mg and Si, increases as $X_{Fe}$ rises from 0 to 10 mol%. However, a decrease in reactivity is observed when $X_{Fe}$ reaches 30 mol%. The reactivity then increases with maximum at $X_{Fe}$ = 45 mol%, and then declines again when $X_{Fe}$ increases to 50 mol%. Figure 6C highlights the exceptionally high solubility of Fe in the G05 glass compared to the other samples, which exhibit lower Fe solubility. Overall, these results suggest that introducing Fe enhances the reactivity of magnesium-based glasses. Additionally, the elemental solubility data, presented as the percentage of each dissolved element, is provided in Supplementary Material S7. The data reveal all glasses with varying Fe concentrations exhibit Si solubility higher than 60 mol%, with Si solubility exceeding 80 mol% in the sample with $X_{Fe}$ = 45 mol%. This indicates the high reactivity of the synthetic glasses in this study. In the following sections, we will explore how $Fe^{3+}$ incorporation influences overall reactivity based on the physico-chemical characterizations of the materials. We provide insights on the role of $Fe^{3+}$ in the glass network, aiming to better understand the structural factors driving reactivity changes and optimize compositions for more reactive glass systems.

## 3.4 Structural analysis of glasses

### 3.4.1 DSC investigation on glass thermal stability

The thermal stability of glasses is assessed from the glass transition temperature ($T_g$) and the glass crystallization temperature ($T_c$, maximum of the crystallization peak), both of which are obtained from DSC data. The $T_g$ implies the onset of polymer chain mobility in amorphous materials, observed as a slight change in the slope of the heat flow curve (Leyva-Porras et al., 2019), while $T_c$ is marked by exothermic events (Senkov et al., 2002). Generally, $T_g$ reflects the degree of crosslinking in the glass structure (Naito and Miura, 1993; Kozmidis-Petrović, 2010), with a decrease often linked to the disruption of Si-O-Si bonds (Le Losq and Neuville, 2013). Materials with higher $T_g$ and $T_c$ require higher activation energy for atomic motion and exhibit higher thermal stability (Lankhorst, 2002) (Supplementary Material S8).

DSC curves shown in Figure 7 provide information on $T_g$ and $T_c$ of glass samples. Figure 7A shows that all Fe-bearing glasses exhibit

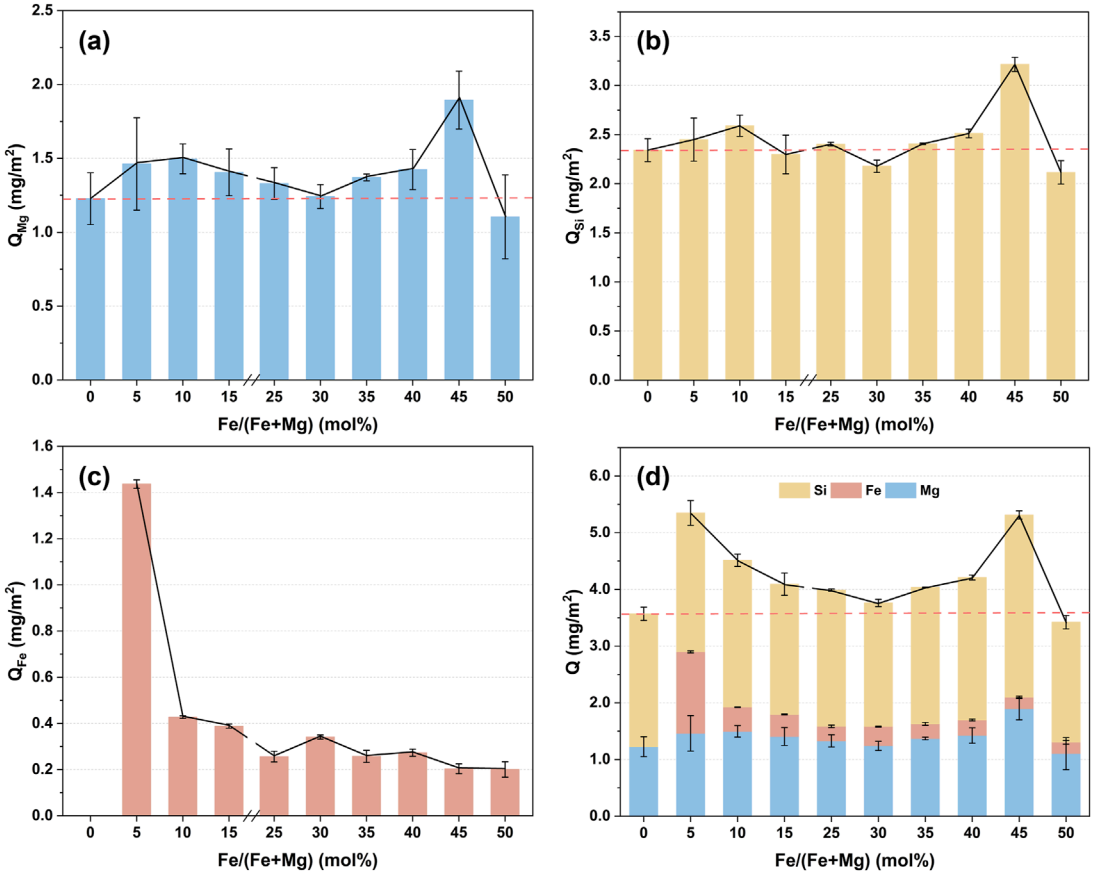


FIGURE 6
Reactivity of glasses assessed by normalized mass loss ($Q_i$) of **(A)** Mg, **(B)** Si, **(C)** Fe, and **(D)** total normalized elemental mass loss. Variation is based on duplicate batch results. The pH of the leachates ranges between 9.5 and 9.8 (Supplementary Material S6).

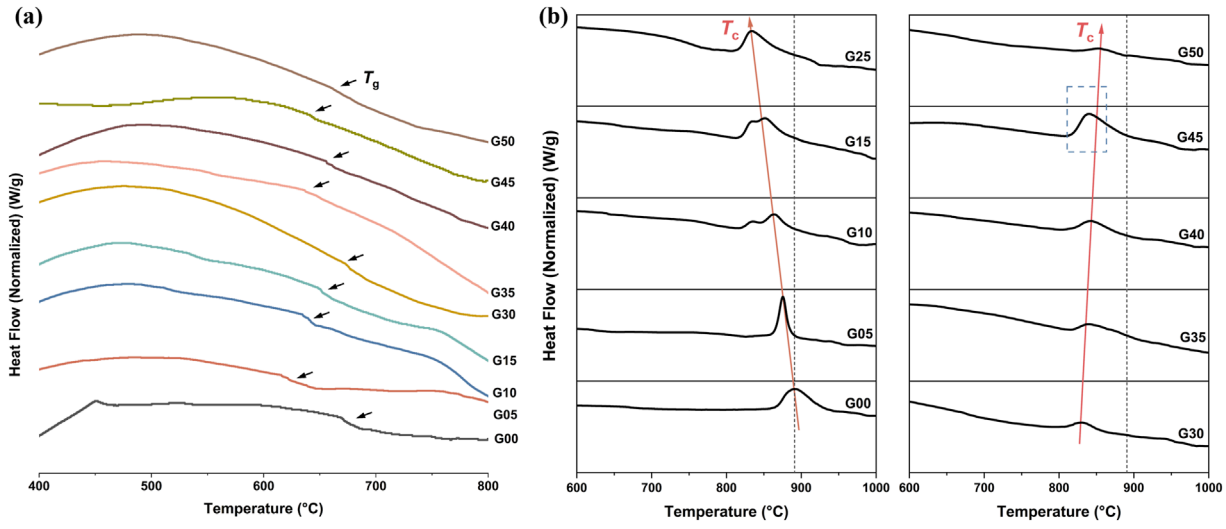


FIGURE 7
DSC patterns for glasses with different Fe contents including the information of **(A)** glass transition temperature $T_g$, and **(B)** glass crystallization temperature $T_c$. The black short-dashed line in **(B)** indicates the crystallization point of the reference sample G00. All glasses doped with Fe show lower $T_g$ and lower $T_c$ compared to Mg-Si glasses (G00).

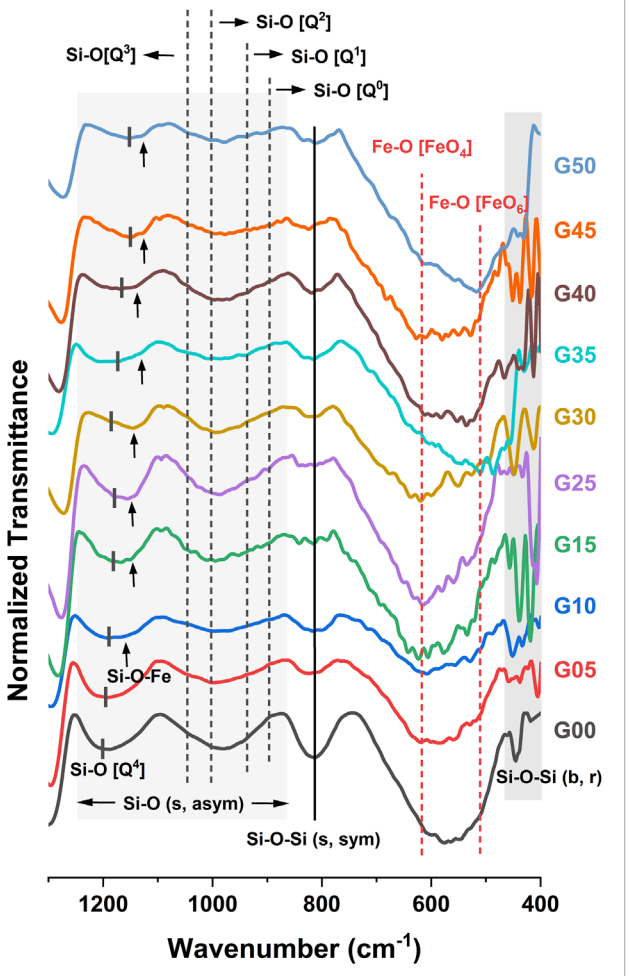


FIGURE 8
FTIR spectra for G00-G50 glasses.

lower $T_g$ than binary Mg-Si glasses ($X_{Fe} = 0$), suggesting that glasses doped with Fe have lower cross-linking degree than glasses without Fe, and they require lower activation energy for atomic movement. The stability of glasses deteriorates rapidly with the introduction of Fe, as seen by the significant decline in $T_g$ when $X_{Fe}$ increases from 0% to 5%, contributing to the high solubility of Fe for the G05 sample. However, the glass transition temperatures fluctuate non-linearly with increasing Fe contents. It can be observed in Figure 7B that $T_c$ decreases with increasing $X_{Fe}$ from 0% to 25%. Conversely, $T_c$ shows a trend to increase when $X_{Fe}$ exceeds 25%. G45 glass breaks this tendency and has a lower $T_c$ value than G40 glass, which explains why G45 samples show higher solubility compared to other samples. Similarly, all glasses doped with Fe exhibit lower $T_c$ than G00 glass. In agreement, small peaks observed in XRD data of G30 and G35 glasses are aligned with the low $T_c$ of these two samples. To summarize, the introduction of Fe in Mg-Si glasses weakens network connectivity, in agreement with the higher ion solubility of Fe-bearing glasses.

### 3.4.2 FTIR characterization

FTIR spectroscopy was employed to investigate the chemical environment governing the bonds formation in the glass samples, and the obtained spectra are shown in Figure 8. The band between 1,300 and 850 $cm^{-1}$ is assigned to antisymmetric vibration of Si-O bonds within [$SiO_4$] comprising diverse $Q^n$ units, where n refers to the number of non-bridging oxygen atoms within glass forming units (from $Q^0$ to $Q^4$) (Ma et al., 2008; Delpino et al., 2021). The band at ~1,190 $cm^{-1}$ in G00 glass is attributed to the Si-O antisymmetric stretching vibrations of bridging oxygens in $Q^4$ structure (Zhao et al., 2016; Luo et al., 2021). The broadening and weakening of bands at 1,250-1,100 $cm^{-1}$ with increasing Fe content is due to the formation of Fe-O-Si bonds at the expense of Si-O-Si bridging units (Van De Leest and Roozeboom, 1998). Bands of M (Si, Fe)-O stretching vibration progressively shift to lower wavenumbers, aligned with previous observations (Yoshio et al., 1981). It has also been suggested that bands shifting to lower wavenumbers implies a smaller degree of crosslinking in [Si-O] networks, which is likely compensated for by the incorporation of [$FeO_4$] and [$SiO_4$] tetrahedra (Glazkova et al., 2015). Generally, the bands at about 1,055 $cm^{-1}$, 1,005 $cm^{-1}$, 945 $cm^{-1}$ and 895 $cm^{-1}$ are assigned to the Si-O vibrations in $Q^3$, $Q^2$, $Q^1$ and $Q^0$ structures (Delpino et al., 2021; Luo et al., 2021). The band at ~820 $cm^{-1}$ relates to Si-O-Si symmetric stretching vibration (Yoshio et al., 1981). The intensity bands associated to the vibrational modes of Si-O bonds decreases with increasing Fe content due to breakage of Si-O bonds and replacement of Si-O-Si by Fe-O-Si (Atalay et al., 2001). The bands between 470 and 400 $cm^{-1}$ are attributed to an overlap of Si-O-Si bending and rocking vibrations (Ma et al., 2008; 2011; Fneich et al., 2018).

Vibrations of Fe-O bonds in [$FeO_4$] tetrahedra and [$FeO_6$] octahedra are observed at ~620 $cm^{-1}$ and ~510 $cm^{-1}$, respectively (Iordanova et al., 1996; Rada et al., 2011; Glazkova et al., 2015). When Fe is introduced, an intense Fe-O band associated with [$FeO_4$] units is observed in the G05 glass in Figure 8, suggesting that a significant proportion of $Fe^{3+}$ ions occupy tetrahedral sites at low concentrations. These [$FeO_4$] groups cross-link the Si chains and act as network formers (Misbah et al., 2021). When $X_{Fe}$ exceeds 30%, the bands at 650-450 $cm^{-1}$ shift to lower wave numbers, which indicate a gradual transition from [$FeO_4$] tetrahedra to [$FeO_6$] octahedra (Baowei et al., 2013b).

### 3.4.3 XPS analysis

XPS analysis was conducted to investigate the glass structure by examining the binding energies of Si 2p and O 1s, providing insights into the bonding environment. The XPS Si 2p and O 1s spectra for G05, G15, G35 and G45 glasses are shown in Figure 9. The spectra show a Si 2p peak ranging from 102.3 to 103.5 eV, aligning well with other multi-oxide silicate materials (Sawyer et al., 2012; Stone-Weiss et al., 2020). Si is primarily found in two forms: bonded with bridging oxygens [Si-O-Si (Fe)] and bonded with non-bridging oxygens [Si-O-Mg (Fe)] (Simonsen et al., 2009). In Figure 9A, as $X_{Fe}$ transitions from 5% to 15%, there is a noticeable increase in binding energy of Si 2p. However, when $X_{Fe}$ reaches 35%, the binding energy decreases. The Si 2p peak shift occurs due to changes in the electron density surrounding the Si atom, which result from varying chemical environments (Zhao et al., 2016). The Si 2p binding energy varies slightly among each species ($Q^n$), with Si species exhibiting lower polymerization typically found at lower binding energy levels (Dalby et al., 2007). The deconvolution of Si 2p spectra is provided in Supplementary Material S9, where $Q^4$,

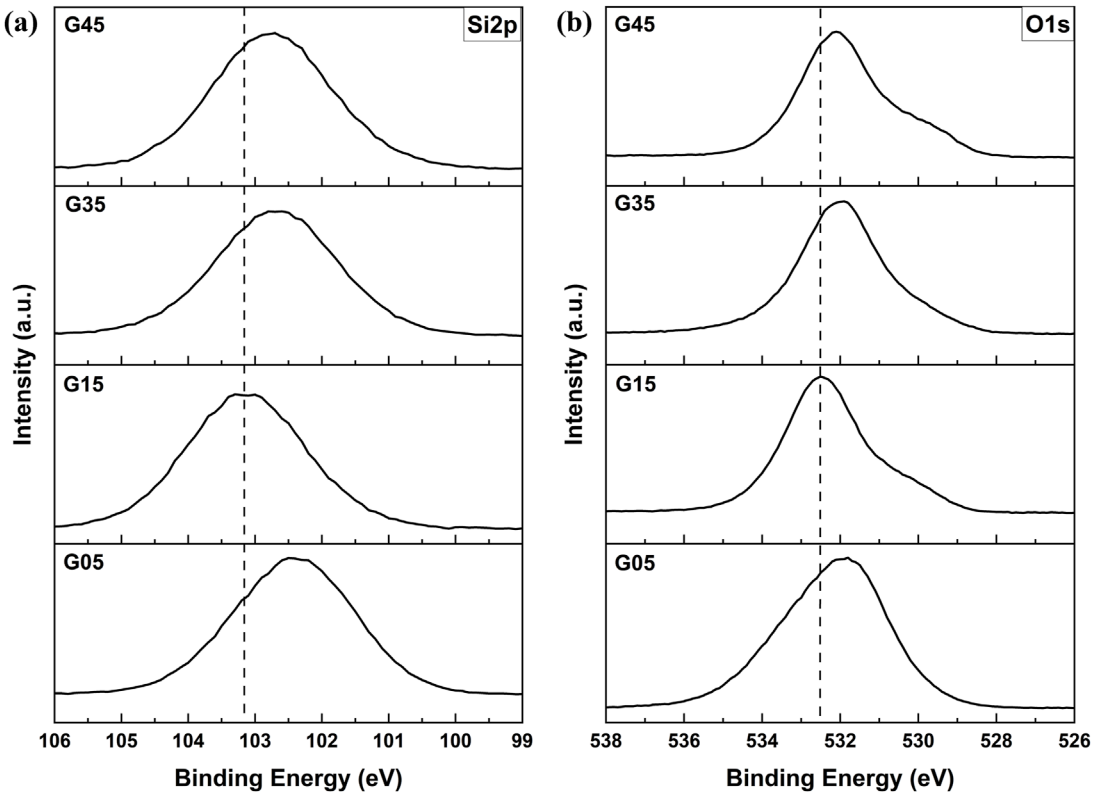


FIGURE 9
**(A)** Si 2p spectra and **(B)** O 1s spectra of G05, G15, G35 and G45 glasses. Vertical dashed lines indicate the highest binding energies observed among the tested samples.

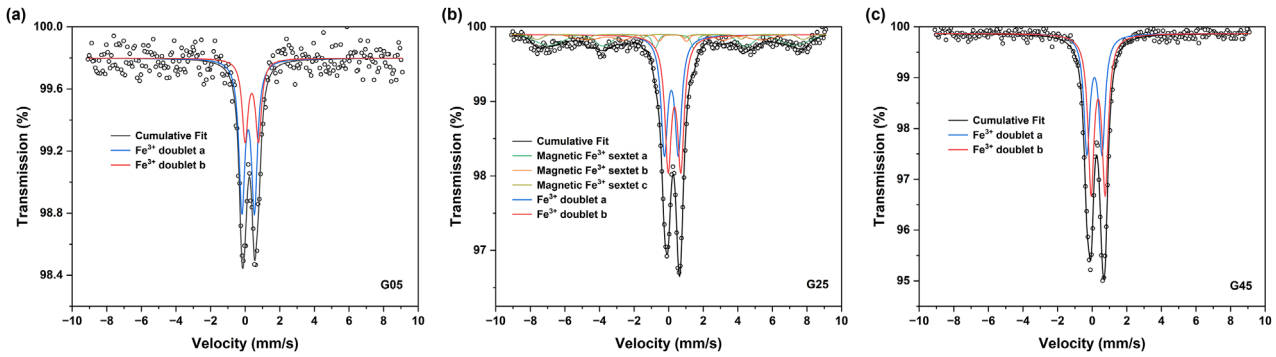


FIGURE 10
Mössbauer spectra of **(A)** G05, **(B)** G25 and **(C)** G45 glasses measured at room temperature. All samples exhibit two distinct paramagnetic $Fe^{3+}$ doublets, and the G25 glass also shows minor magnetic $Fe^{3+}$ sextets.

$Q^3$ and $Q^2$ species are fitted, and the relative area ratios for each species are presented. Among the samples, the G15 glass exhibits the highest fraction of highly polymerized Si species ($Q^4$ = 17.0%) and the lowest fraction of depolymerized $Q^2$ species ($Q^2$ = 8.9%). Combined with its higher binding energy value, this indicates that G15 has a more cross-linked and polymerized network structure compared to other samples. In contrast, the G45 glass contains the highest fraction of depolymerized $Q^2$ species ($Q^2$ = 16.1%), and the greatest overall proportion of less polymerized Si species ($Q^{2-3}$ = 89.1%), followed by G35 ($Q^2$ = 14.6%, $Q^{2-3}$ = 87.6%) and G05 ($Q^2$ = 13.0%, $Q^{2-3}$ = 85.5%). Additionally, the lower binding energies of Si 2p in G35 and G45 further suggest a weakening in structural connectivity, pointing to a less polymerized network compared to G15. These observations align with the observations in FTIR spectra, which may be associated with a gradual transition from [$FeO_4$] tetrahedra to [$FeO_6$] octahedra. Specifically, in the G05 sample, the low binding energy of Si 2p and high ratio of $Q^3$ and $Q^2$ species might be attributed to the high concentration

TABLE 3 Mössbauer parameters for G05, G25 and G45 glasses at room temperature: isomer shift ($\delta$), quadrupole splitting ($\Delta E_Q$), line width ($\Gamma$), and tetrahedral-to-octahedral component ratios.

| | | G05 | G25 | G45 |
|---|---|---|---|---|
| $Fe^{3+}$ doublet a | $\delta$ (mm/s) | 0.21 ± 0.01 | 0.27 ± 0.01 | 0.24 ± 0.01 |
| | $\Delta E_Q$ (mm/s) | 1.44 ± 0.03 | 1.62 ± 0.04 | 1.76 |
| | $\Gamma$ (mm/s) | 0.41 ± 0.03 | 0.46 ± 0.01 | 0.43 |
| $Fe^{3+}$ doublet b | $\delta$ (mm/s) | 0.49 ± 0.01 | 0.45 ± 0.01 | 0.46 |
| | $\Delta E_Q$ (mm/s) | 1.55 ± 0.05 | 1.47 | 1.63 |
| | $\Gamma$ (mm/s) | 0.41 ± 0.03 | 0.46 ± 0.01 | 0.43 |
| $Fe^{3+}$ (Td)/$Fe^{3+}$ (Oh) | | 1.83 | 0.89 | 0.75 |

of MgO modifiers, agreeing with the low $T_g$ value of G05 in DSC analysis.

O 1s peaks of G05, G15, G35 and G45 glasses are observed between 531.7 and 532.5 eV in Figure 9B. The binding energy increases as $X_{Fe}$ transitions from 5% to 15%, while a shift toward a lower binding energy value is seen when $X_{Fe}$ reaches 35%. Based on the previous investigation, the O species with low binding energy are interpreted as non-bridging oxygen [Si-O-Mg (Fe)], while high energy species correspond to the bridging oxygen [Si-O-Si (Fe)] (Gresch et al., 1979). Prior studies support that the O-Si bond is less ionic compared to O-Fe and O-Mg (Barr, 1990; Scholtzová et al., 2000; Yliniemi, 2022). Hence, the binding energy of O 1s decreases as O-Si is gradually substituted by O-Fe with the increase of Fe content. Additionally, the decrease in O 1s binding energy indicates that the fraction of non-bridging oxygen increases, which further implies the change of Fe coordination number in networks.

### 3.4.4 Mössbauer spectra

Mössbauer spectroscopy was conducted to determine the chemical environments of Fe in the glass structure. Three glass samples G05, G25 and G45 were analyzed, and the resulting spectra are shown in Figure 10. Circles indicate the raw experimental data, while continuous lines represent the fitted data. Each sample exhibits two paramagnetic trivalent iron doublets with distinct isomer shifts, represented by blue and red lines. These doublets provide an averaged view of the possible paramagnetic $Fe^{3+}$ environments within the glasses, associated with different coordination geometries (Kurkjian, 1970). The broad peaks and relatively large quadrupole splitting of the doublets reflect the amorphous nature of glasses; the absence of a well-defined crystal structure results in a distribution of hyperfine parameters (Horie et al., 1978). Notably, magnetic trivalent iron sextets (similarly to $Fe_2O_3$), are observed in the G25 glass, while a close inspection of the G45 spectrum suggests a small amount of similar magnetic iron, although in insufficient quantities for reliable fitting.

The isomer shift ($\delta$, corrected with metallic α-iron at room temperature), quadrupole splitting ($\Delta E_Q$) and line width ($\Gamma$) for each glass sample are summarized in Table 3. The isomer shift is primarily associated with the $^{57}Fe$ absorption, reflecting variations in electron density at the nucleus due to differing chemical environments, causing slight shifts in velocity (Kistner and Sunyar, 1960; Walker et al., 1961). An isomer shift around 0.26 mm/s typically indicates $Fe^{3+}$ in a tetrahedral coordination, while higher velocities near 0.5 mm/s correspond to octahedrally coordinated $Fe^{3+}$ (Coey, 1974; Horie et al., 1978; Mysen, 1987; Xu et al., 2024). Therefore, all three glass samples exhibit both tetrahedral (doublet a) and octahedral (doublet b) coordinated $Fe^{3+}$, with $\Delta E_Q$ near or above 1.5 mm/s, indicating some degree of distortion (Sharma et al., 2007; Xu et al., 2024). The broad line widths suggest a distribution of $Fe^{3+}$ environments within the glass. The ratios of tetrahedral to octahedral components are also provided in Table 3. The G05 glass exhibits the highest proportion of tetrahedrally coordinated $Fe^{3+}$, which decreases in the G25 glass as the proportion of octahedrally coordinated $Fe^{3+}$ increases, while the G45 glass showing the highest proportion of $Fe^{3+}$ in octahedral coordination. These results are also aligned with the evidence found in the FTIR analysis, indicating that higher Fe concentrations favor the formation of [$FeO_6$] units and drive the conversion of [$FeO_4$] to [$FeO_6$] coordination.

### 3.4.5 Impacts of $Fe^{3+}$ on the structure and reactivity of Mg-Si glasses

In Fe-free Mg silicate glass, $Mg^{2+}$ acts as a network modifier within the glass structure, as illustrated in Figure 11A. When Fe is introduced into the glass network, $Fe^{3+}$ ions substitute $Si^{4+}$ and primarily form [$FeO_4$] tetrahedra connected to bridging oxygens. This is indicated by FTIR analysis, which shows a wavenumber shift from Si-O-Si to Si-O-Fe upon Fe incorporation. If [$FeO_4$] tetrahedra units replace the [$SiO_4$] units, they generate a negative charge deriving from the isomorphous replacement of $Si^{4+}$ with $Fe^{3+}$ (Holland et al., 1999). This requires a modifier cation to be close by for local charge compensation (Kalahe et al., 2022). The expected chemical environment of $Fe^{3+}$ and $Mg^{2+}$ ions is shown in Figure 11B. In the glasses systems investigated in this work, it is expected to have enough $Mg^{2+}$ to charge-compensate [$FeO_4$] at systems with low $Fe^{3+}$ concentrations, which would lead to a minimal variation in the mobility of $Mg^{2+}$. Although tetrahedrally coordinated $Fe^{3+}$ ions are expected to act as network formers, introducing $Fe^{3+}$ into the system likely destabilizes the network and reduces connectivity due to the weaker bond strength of Fe-O. This is supported by DSC analysis, where G05 glass exhibits a significantly lower $T_g$ compared to the Fe-free G00 glass. Additionally, the relatively low binding energies of Si 2p and O 1s suggest weak network connectivity. Consequently, the solubility of Si and Mg in the G05 glass is still enhanced relative to that in the G00 glass.

Remarkably, G05 glass shows exceptionally high leachability of Fe, which could be explained based on the STEM analysis (Figure 12). A clear droplet phase separation is observed in the Fe map shown in Figure 12A, suggesting that Fe is proportionally immiscible with magnesium silicate phases. The droplet-separated phase is seen as an amorphous structure in the STEM diffraction analysis (Figure 12B). Thus, these 50–100 nm droplets seem to be formed of Fe-rich glass and distributed on Fe-poor glass matrix, significantly enhancing Fe leachability. Additionally, the Fe-rich glass is expected to contain a significant proportion of network modifier [$FeO_6$] units, contributing to the overall increased reactivity of the G05 glass compared to the G00 glass. Similarly,

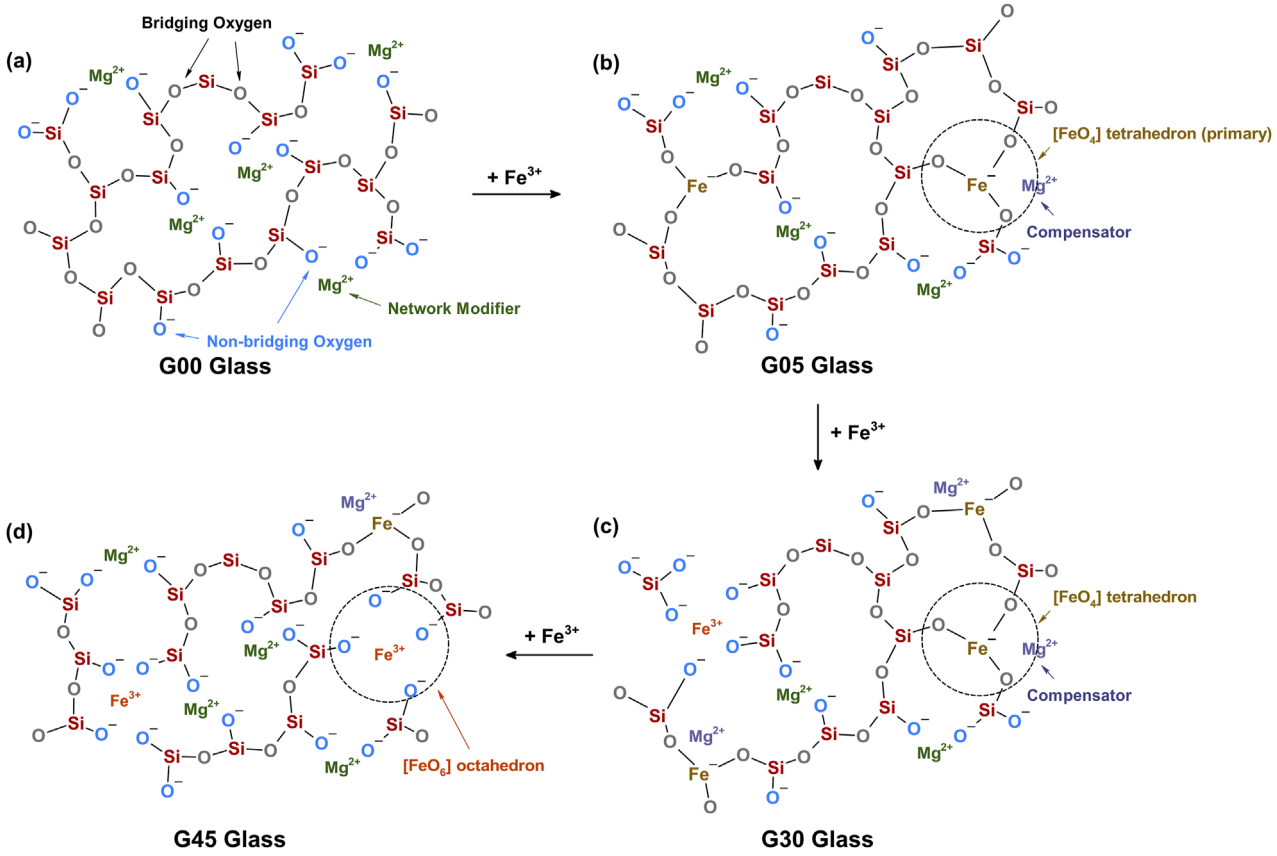


FIGURE 11
2D schematic presentation of the $Fe^{3+}$-Mg silicate glass networks. **(A)** In the G00 glass, $Mg^{2+}$ acts as the network modifier, weakly bonding to non-bridging oxygens. **(B)** With the introduction of $Fe^{3+}$ in the G05 glass, [$FeO_4$] tetrahedra primarily form and act as the network formers, while some $Mg^{2+}$ ions transition from the network modifier to the charge compensator at low Fe concentrations. **(C)** As Fe concentrations increase, more $Mg^{2+}$ ions function as compensators, as shown in the G30 glass. **(D)** In the G45 glass, a higher proportion of [$FeO_4$] tetrahedra convert into [$FeO_6$] octahedra, acting
as network modifiers.

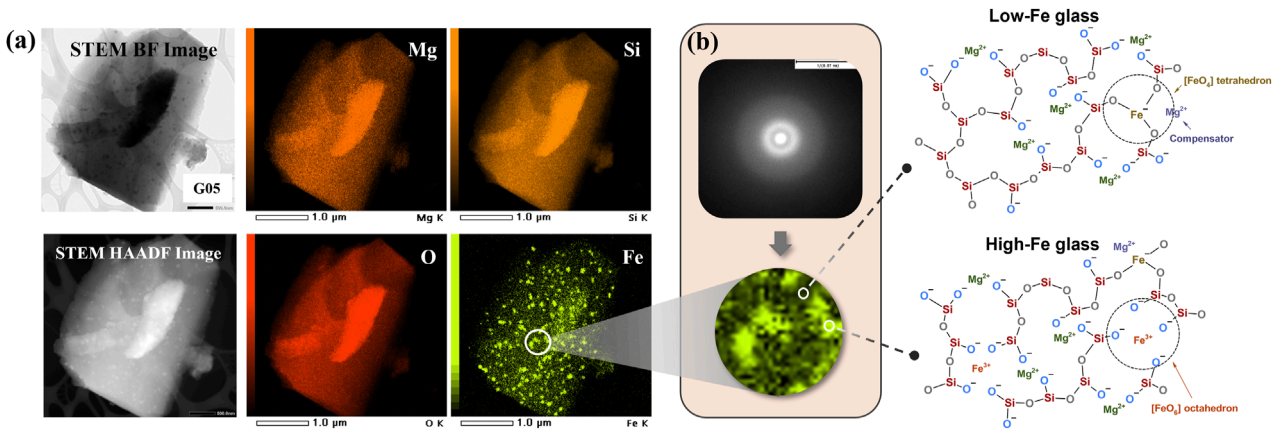


FIGURE 12
STEM images of the G05 glass and maps of Mg, Si, O and Fe. Droplet phase separation is observed in **(A)** Fe map, mainly composed of iron-rich glass, which is separated into ~50-100 nm-sized droplets dispersed in the Fe-poor main glass. The amorphous structure shown in **(B)** STEM diffraction analysis supports the existence of phase separation in glasses.

droplet-like phase separation of Fe is observed in STEM images of the G10 glass, but less pronounced than in the G05 glass. In the G50 glass, phase separation is also evident, with Si and Mg notably depleted in Fe-rich regions (Supplementary Material S10). These observations may infer that increasing Fe concentration facilitates the segregation of Fe-rich and Si-rich phases, which may explain the enhanced dissolution of Si and Mg as illustrated in Figure 6. Thus, the phase immiscibility in $Fe^{3+}$-Mg silicate glasses may also contribute to the enhanced reactivity of Fe-doped samples compared to binary magnesium silicate glasses.

When $X_{Fe}$ increases from 5% to 30%, some [$FeO_4$] units convert to [$FeO_6$], as indicated in Mössbauer spectra showing a higher fraction of [$FeO_6$] in G25 compared to the G05 glass. Nevertheless, the overall amount of [$FeO_4$] units in the glass network likely increases, as seen in FTIR spectra where both Fe-O bands for [$FeO_4$] and [$FeO_6$] increase, with a more pronounced rise in [$FeO_4$] intensity in G15 and G25 glasses. This would shift more $Mg^{2+}$ ions to the role of compensators instead of modifier cations, thereby enhancing the polymerization degree of the glass network. XPS analysis supports this interpretation, with G15 showing the highest binding energy of Si 2p and O 1s, and the largest proportion of polymerized $Q^4$ species through deconvolution analysis. This increased polymerization may account for the modest decrease in the ionic leaching ratio. The anticipated chemical environments of $Fe^{3+}$ and $Mg^{2+}$ ions in the G30 glass are illustrated in Figure 11C.

As $X_{Fe}$ continues to increase, the amount of $Fe^{3+}$ acting as a network former is limited by the Si to Fe ratio, as Fe-O bonds are less stable than Si-O bonds (Arslan et al., 2009). Higher $Fe^{3+}$ concentrations would favor further conversion of [$FeO_4$] tetrahedra to [$FeO_6$] octahedra (Figure 11D), as indicated by Mössbauer spectra for the G45 glass, which shows the highest fraction of octahedrally coordinated $Fe^{3+}$. Given that [$FeO_6$] octahedra act as network modifiers and promote network depolymerization (Pinakidou et al., 2007), with a continuous increase of $X_{Fe}$, a more open structure and a reduced level of polymerization within the network are expected. This is supported by XPS analysis, where G35 and G45 glasses show significantly lower binding energies of Si 2p and O 1s, with G45 exhibiting the highest proportion of depolymerized $Q^2$ and $Q^3$ species. This increased depolymerization contributes to the enhanced reactivity of the glasses. The decrease in the dissolution observed for the G50 glass may be attributed to a higher degree of crystallinity, seen in the minor reflections in the XRD patterns (Nommeots-Nomm et al., 2020).

Overall, these findings reveal that $Fe^{3+}$ significantly impacts the reactivity of Mg-Si glasses, with its primary role as network former or modifier depending on the glass composition. Structural changes observed in Mössbauer, XPS, DSC and FTIR analyses demonstrate a clear relationship between Fe concentration and reduced glass connectivity, with additional observation of phase separation seen in STEM figures.

## 4 Conclusion

This study reported the synthesis of Fe-bearing magnesium silicate glasses with varying Fe content via a sol-gel method, and an investigation of their reactivity through solubility behavior analysis. Samples with $X_{Fe}$ [Fe/(Fe + Mg)] up to 50 mol% exhibited an amorphous structure, according to the observations in the XRD measurements. The incorporation of Fe into Mg-Si glasses resulted in a significant enhancement in reactivity compared to previously studied Mg-Si glasses (Jiang et al., 2023). This increase is attributed primarily to the weakening of network connectivity and the reduction of structural stability caused by the presence of Fe. At low Fe concentration ($X_{Fe}$ = 5%–10%), $Fe^{3+}$ ions are believed to replace $Si^{4+}$, primarily forming [$FeO_4$] tetrahedra connected to bridging oxygens and acting as network formers. However, it is possible that the relatively weaker Fe-O bonds destabilized the network, along with the formation of nanoscale phase separation into iron-rich and iron-poor regions, as observed in STEM-EDS analysis, promoting elemental dissolution, particularly the leaching of Fe. When the Fe concentrations increased, FTIR and XPS analyses indicated a gradual transition of [$FeO_4$] tetrahedra to [$FeO_6$] octahedra, with Mössbauer spectra of representative samples showing this transition at higher Fe concentrations. Interestingly, as $X_{Fe}$ increased from 10% to 30%, a slight decrease in reactivity was observed, possibly due to a partial shift of $Mg^{2+}$ from a network modifier to a charge compensator. This led to an increase in network polymerization, which was only minimally offset by the addition of [$FeO_6$] units. XPS analysis, through deconvolution, supports this interpretation, showing that the G15 glass exhibited a more polymerized structure compared to the G05, G35 and G45 glasses. The notable increase in reactivity beyond $X_{Fe}$ = 30% is attributed to the higher concentration of [$FeO_6$] octahedra acting as network modifiers, leading to further depolymerization of the glass network and a consequent enhancement in reactivity. The high Si solubility of the glasses, with all samples showing over 60 mol% and exceeding 80 mol% for the glass with $X_{Fe}$ = 45%, indicates the potential for high reactivity of the synthetic $Fe^{3+}$-Mg silicate glasses.

The study provides useful insights into the potential of Fe-bearing magnesium silicate glasses as effective supplementary cementitious materials (SCMs). The ability to fine-tune the reactivity of these glasses through controlled Fe incorporation offers a promising pathway for developing SCMs that can contribute to reducing $CO_2$ emissions in cement production. Additionally, this understanding opens possibilities for utilizing and modifying highly available resources, such as Fe- and Mg-rich inorganic waste streams, glass waste, mine tailings, and Mg silicates, to produce reactive materials for SCM applications. While reactivity is largely influenced by the chemical composition, it may not be strictly dependent on preparation method, suggesting that optimized glass compositions achieved via sol-gel processing may also be adapted for materials produced by other methods. Follow-up research could tackle the use of variable feedstocks for producing Mg silicate glasses and investigate their use as SCMs in construction materials.

## Data availability statement

The original contributions presented in the study are included in the article/Supplementary Material, and the raw data of all characterization done in the manuscript is openly available at Zenodo with the following DOI number: 10.1016/j.jobe.2021.103699, complying to the FAIR principles of the Research Council of Finland.

## Author contributions

CJ: Conceptualization, Formal Analysis, Investigation, Methodology, Writing - original draft, Writing - review and editing. HS: Investigation, Supervision, Writing - review and editing, Validation. JY: Funding acquisition, Investigation, Methodology, Supervision, Writing - review and editing. JL: Methodology, Formal analysis, Investigation, Software, Writing - review and editing. DR: Conceptualization, Investigation, Methodology, Supervision, Writing - review and editing. MI: Funding acquisition, Supervision, Writing - review and editing. CC: Investigation, Supervision, Writing - review and editing. PK: Conceptualization, Funding acquisition, Investigation, Methodology, Project administration, Supervision, Validation, Writing - review and editing.

## Funding

The author(s) declare that financial support was received for the research, authorship, and/or publication of this article. The authors gratefully acknowledge the financial support received from Research Council of Finland (grants 322085 and 354263) and the University of Oulu and the Research Council of Finland Profi5 (326291). This work was partially funded by the University of Oulu Kvantum Institute CARBO-CEM project. HS and PK acknowledge the financial support from the Research Council of Finland (funding decision 347183). Part of the work was carried out with the support of the Centre for Material Analysis, University of Oulu, Finland.

## Acknowledgments

The authors wish to thank Marcin Selent for his help with XRD analysis, Tommi Kokkonen with DSC measurement, Pasi Juntunen with FESEM measurement, Kaisu Ainassaari with SSA analysis, Jarno Karvonen with PSD and TG measurements, Jani Österlund with ICP measurement, Sami Saukko with STEM measurement, Leena Palmu with XRF measurement, Santtu Heinilehto with XPS measurement. Jarno Karvonen, Jani Österlund and Elisa Wirkkala are acknowledged for their contribution to laboratory assistance.

## Conflict of interest

The authors declare that the research was conducted in the absence of any commercial or financial relationships that could be construed as a potential conflict of interest.

The author(s) declared that they were an editorial board member of Frontiers, at the time of submission. This had no impact on the peer review process and the final decision.

## Generative AI statement

The author(s) declare that no Generative AI was used in the creation of this manuscript.

## Publisher's note



## Supplementary material

The Supplementary Material for this article can be found online at: https://www.frontiersin.org/articles/10.3389/fmats.2024.1509403/full#supplementary-material

## References

Alzeer, M. I. M., Cheeseman, C., and Kinnunen, P. (2022a). New synthetic glass-based supplementary cementitious materials derived from basalt composition. *J. Build. Eng.* 46, 103699. doi:10.1016/j.jobe.2021.103699

Alzeer, M. I. M., Nguyen, H., Fabritius, T., Sreenivasan, H., Telkki, V.-V., Kantola, A. M., et al. (2022b). On the hydration of synthetic aluminosilicate glass as a sole cement precursor. *Cem. Concr. Res.* 159, 106859. doi:10.1016/j.cemconres.2022.106859

Aminirastabi, H., Xue, H., Peng, D., Ji, G., Aminirastabi, H., Xue, H., et al. (2018). "Sol-gel process and engineering nanostructure," in *Sol-gel method - design and synthesis of New materials with interesting physical, chemical and biological properties* (London, United Kingdom: IntechOpen). doi:10.5772/intechopen.79857

Arslan, G., Dölekçekiç, E., and Karasu, B. (2009). Effect of transition metal oxide additions on the chemical durability of SrOMgOZrO2SiO2 glasses. *Eur. J. Glass Sci. Technol. Part A*. Available at: https://www.academia.edu/32370386/Effect_of_transition_metal_oxide_additions_on_the_chemical_durability_of_SrOMgOZrO2SiO2_glasses.

Atalay, S., Adiguzel, H. I., and Atalay, F. (2001). Infrared absorption study of Fe2O3–CaO–SiO2 glass ceramics. *Mat. Sci. Eng. A* 304–306, 796–799. doi:10.1016/S0921-5093(00)01572-0

Baccile, N., Babonneau, F., Thomas, B., and Coradin, T. (2009). Introducing Ecodesign in silica sol–gel materials. *J. Mat. Chem.* 19, 8537–8559. doi:10.1039/B911123A

Baino, F., Fiume, E., Miola, M., Leone, F., Onida, B., Laviano, F., et al. (2018). Fe-doped sol-gel glasses and glass-ceramics for magnetic hyperthermia. *Materials* 11, 173. doi:10.3390/ma11010173

Baowei, L., Leibo, D., Xuefeng, Z., and Xiaolin, J. (2013a). Structure and performance of glass–ceramics obtained by Bayan Obo tailing and fly ash. *J. Non-Cryst. Solids* 380, 103–108. doi:10.1016/j.jnoncrysol.2013.09.012

Baowei, L., Yongsheng, D., Xuefeng, Z., Ming, Z., and Hua, C. (2015). Crystallization characteristics and properties of high-performance glass-ceramics derived from baiyunebo east mine tailing. *Environ. Prog. Sustain. Energy* 34, 420–426. doi:10.1002/ep.12006

Baowei, L., Yongsheng, D., Xuefeng, Z., Xiaolin, J., Ming, Z., and Hua, C. (2013b). Effects of iron oxide on the crystallization kinetics of baiyunebo tailing glass-ceramics. *Trans. Indian Ceram. Soc.* 72, 119–123. doi:10.1080/0371750X.2013.795718

Barr, T. L. (1990). The nature of the relative bonding chemistry in zeolites: an XPS study. *Zeolites* 10, 760–765. doi:10.1016/0144-2449(90)90058-Y

Catauro, M., Dell'Era, A., and Vecchio Ciprioti, S. (2016). Synthesis, structural, spectroscopic and thermoanalytical study of sol–gel derived SiO2–CaO–P2O5 gel and ceramic materials. *Thermochim. Acta* 625, 20–27. doi:10.1016/j.tca.2015.12.004

CEMBUREAU (2020). From Ambition to Deployment - our 2050 roadmap. *CEMBUREAU*. Available at: https://cembureau.eu/media/ulxj5lyh/cembureau-net-zero-roadmap.pdf.

Cheng, X., Brow, R. K., and Chen, G. (2017). The dissolution behavior in alkaline solutions of a borosilicate glass with and without P2O5. *J. Am. Ceram. Soc.* 100, 4519–4532. doi:10.1111/jace.14933

Coey, J. M. D. (1974). Amorphous solids: a review of the applications of the mössbauer effect. *J. Phys. Colloq.* 35, 89–105. doi:10.1051/jphyscol:1974608

Corkhill, C. L., Cassingham, N. J., Heath, P. G., and Hyatt, N. C. (2013). Dissolution of UK high-level waste glass under simulated hyperalkaline conditions of a colocated geological disposal facility. *Int. J. Appl. Glass Sci.* 4, 341–356. doi:10.1111/ijag.12042

Coroiu, I., Culea, E., and Darabont, A. (2005). Magnetic and structural behaviour of the sol–gel-derived iron aluminosilicate glass-ceramics. *J. Magn. Magn. Mat.* 290–291, 997–1000. doi:10.1016/j.jmmm.2004.11.308

Dalby, K. N., Nesbitt, H. W., Zakaznova-Herzog, V. P., and King, P. L. (2007). Resolution of bridging oxygen signals from O 1s spectra of silicate glasses using XPS: implications for O and Si speciation. *Geochim. Cosmochim. Acta* 71, 4297–4313. doi:10.1016/j.gca.2007.07.005

Delpino, G. P., Borges, R., Zambanini, T., Joca, J. F. S., Gaubeur, I., de Souza, A. C. S., et al. (2021). Sol-gel-derived 58S bioactive glass containing holmium aiming brachytherapy applications: a dissolution, bioactivity, and cytotoxicity study. *Mat. Sci. Eng. C* 119, 111595. doi:10.1016/j.msec.2020.111595

Deng, X., Guo, H., Tan, H., Nie, K., He, X., Yang, J., et al. (2022). Effect of organic alkali on hydration of GGBS-FA blended cementitious material activated by sodium carbonate. *Ceram. Int.* 48, 1611–1621. doi:10.1016/j.ceramint.2021.09.240

Diamond, S. (1983). On the glass present in low-calcium and in high-calcium flashes. *Cem. Concr. Res.* 13, 459–464. doi:10.1016/0008-8846(83)90002-9

Dislich, H. (1986). Sol-gel: science, processes and products. *J. Non-Cryst. Solids* 80, 115–121. doi:10.1016/0022-3093(86)90384-4

Durdziński, P. T., Snellings, R., Dunant, C. F., Haha, M. B., and Scrivener, K. L. (2015). Fly ash as an assemblage of model Ca–Mg–Na-aluminosilicate glasses. *Cem. Concr. Res.* 78, 263–272. doi:10.1016/j.cemconres.2015.08.005

Enju, S., Kawano, H., Tsuchiyama, A., Kim, T. H., Takigawa, A., Matsuno, J., et al. (2022). Condensation of cometary silicate dust using an induction thermal plasma system - II. Mg–Fe–Si–O–S system and the effects of sulfur and redox conditions. *Astron. Astrophys.* 661, A121. doi:10.1051/0004-6361/202142620

Farges, F., Lefrère, Y., Rossano, S., Berthereau, A., Calas, G., and Brown, G. E. (2004). The effect of redox state on the local structural environment of iron in silicate glasses: a combined XAFS spectroscopy, molecular dynamics, and bond valence study. *J. Non-Cryst. Solids* 344, 176–188. doi:10.1016/j.jnoncrysol.2004.07.050

Figueira, B., Almeida, J. M., Ferreira, B., Coelho, L., and Silva, C. J. (2021). Optical fiber sensors based on sol–gel materials: design, fabrication and application in concrete structures. *Mat. Adv.* 2, 7237–7276. doi:10.1039/D1MA00456E

Fiume, E., Migneco, C., Verne, E., and Baino, F. (2020). Comparison between bioactive sol-gel and melt-derived glasses/glass-ceramics based on the multicomponent SiO2-P2O5-CaO-MgO-Na2O-K2O system. *Materials* 13, 540. doi:10.3390/ma13030540

Fneich, H., Gaumer, N., Chaussedent, S., Blanc, W., and Mehdi, A. (2018). Europium-doped sol-gel SiO2-based glasses: effect of the europium source and content, magnesium addition and thermal treatment on their photoluminescence properties. *Molecules* 23, 1768. doi:10.3390/molecules23071768

Foroutan, F., de Leeuw, N. H., Martin, R. A., Palmer, G., Owens, G. J., Kim, H.-W., et al. (2015). Novel sol–gel preparation of (P2O5)0.4–(CaO)0.25–(Na2O)X–(TiO2)(0.35–X) bioresorbable glasses (X = 0.05, 0.1, and 0.15). *J. Sol-Gel Sci. Technol.* 73, 434–442. doi:10.1007/s10971-014-3555-6

Gartner, E., and Myers, D. (1993). Influence of tertiary alkanolamines on Portland cement hydration. *J. Am. Ceram. Soc.* 76, 1521–1530. doi:10.1111/j.1151-2916.1993.tb03934.x

Glazkova, Ya. S., Kalmykov, S. N., Presnyakov, I. A., Stefanovskaya, O. I., and Stefanovsky, S. V. (2015). The structural state of iron in multicomponent aluminum iron borosilicate glass depending on their composition and synthesis conditions. *Glass Phys. Chem.* 41, 367–377. doi:10.1134/S1087659615040057

Gresch, R., Müller-Warmuth, W., and Dutz, H. (1979). X-ray photoelectron spectroscopy of sodium phosphate glasses. *J. Non-Cryst. Solids* 34, 127–136. doi:10.1016/0022-3093(79)90012-7

Hamdan, A., Hajimohammadi, A., Rawal, A., and Kim, T. (2023). The intrinsic role of network modifiers (Ca versus Mg) in the reaction kinetics and microstructure of sodium silicate-activated CaO-MgO-Al2O3-SiO2 glasses. *Cem. Concr. Res.* 164, 107058. doi:10.1016/j.cemconres.2022.107058

Holland, D., Mekki, A., Gee, I. A., McConville, C. F., Johnson, J. A., Johnson, C. E., et al. (1999). The structure of sodium iron silicate glass – a multi-technique approach. *J. Non-Cryst. Solids* 253, 192–202. doi:10.1016/S0022-3093(99)00353-1

Horie, O., Syono, Y., Nakagawa, Y., Ito, A., Okamura, K., and Yajima, S. (1978). Mössbauer study of amorphous *BaO–Fe2O3–B2O3* system. *Solid State Commun.* 25, 423–426. doi:10.1016/0038-1098(78)90147-3

Iordanova, R., Dimitriev, Y., Dimitrov, V., Kassabov, S., and Klissurski, D. (1996). Glass formation and structure in the V2O5-Bi2O3-Fe2O3 glasses. *J. Non-Cryst. Solids* 204, 141–150. doi:10.1016/S0022-3093(96)00416-4

Jiang, C., Ramteke, D. D., Li, J., Sliz, R., Sreenivasan, H., Cheeseman, C., et al. (2023). Preparation and characterization of binary Mg-silicate glasses via Sol-Gel route. *J. Non-Cryst. Solids* 606, 122204. doi:10.1016/j.jnoncrysol.2023.122204

Juenger, M. C. G., and Siddique, R. (2015). Recent advances in understanding the role of supplementary cementitious materials in concrete. *Cem. Concr. Res.* 78, 71–80. doi:10.1016/j.cemconres.2015.03.018

Kalahe, J., Ono, M., Urata, S., and Du, J. (2022). Composition dependence of the atomic structures and properties of sodium aluminosilicate glasses: molecular dynamics simulations with reactive and nonreactive potentials. *J. Phys. Chem. B* 126, 5326–5342. doi:10.1021/acs.jpcb.2c02292

Kelsey, K. E., Stebbins, J. F., Singer, D. M., Brown, G. E., Mosenfelder, J. L., and Asimow, P. D. (2009). Cation field strength effects on high pressure aluminosilicate glass structure: multinuclear NMR and La XAFS results. *Geochim. Cosmochim. Acta* 73, 3914–3933. doi:10.1016/j.gca.2009.03.040

Kistner, O. C., and Sunyar, A. W. (1960). Evidence for quadrupole interaction of Fe57m, and influence of chemical binding on nuclear gamma-ray energy. *Phys. Rev. Lett.* 4, 412–415. doi:10.1103/PhysRevLett.4.412

Kim, H.-I., and Lee, S. K. (2019). The degree of polymerization and structural disorder in (Mg,Fe)SiO3 glasses and melts: insights from high-resolution 29Si and 17O solid-state NMR. *Geochim. Cosmochim. Acta* 250, 268–291. doi:10.1016/j.gca.2019.02.018

Kinnunen, P., Sreenivasan, H., Cheeseman, C. R., and Illikainen, M. (2019). Phase separation in alumina-rich glasses to increase glass reactivity for low-CO2 alkali-activated cements. *J. Clean. Prod.* 213, 126–133. doi:10.1016/j.jclepro.2018.12.123

Kozmidis-Petrović, A. F. (2010). Sensitivity of the Hruby, Lu–Liu, Fan, Yuan, and Long glass stability parameters to the change of the ratios of characteristic temperatures Tx/Tg and Tm/Tg. *Thermochim. Acta* 510, 137–143. doi:10.1016/j.tca.2010.07.007

Kurkjian, C. R. (1970). Mössbauer spectroscopy in inorganic glasses. *J. Non-Cryst. Solids* 3, 157–194. doi:10.1016/0022-3093(70)90174-2

Kuryaeva, R. G. (2004). Degree of polymerization of aluminosilicate glasses and melts. *Glass Phys. Chem.* 30, 157–166. doi:10.1023/B:GPAC.0000024000.19443.f6

Lankhorst, M. H. R. (2002). Modelling glass transition temperatures of chalcogenide glasses. Applied to phase-change optical recording materials. *J. Non-Cryst. Solids* 297, 210–219. doi:10.1016/S0022-3093(01)01034-1

Le Losq, C., and Neuville, D. R. (2013). Effect of the Na/K mixing on the structure and the rheology of tectosilicate silica-rich melts. *Chem. Geol.* 346, 57–71. doi:10.1016/j.chemgeo.2012.09.009

Leyva-Porras, C., Cruz-Alcantar, P., Espinosa-Solís, V., Martínez-Guerra, E., Piñón-Balderrama, C. I., Compean Martínez, I., et al. (2019). Application of differential scanning calorimetry (DSC) and modulated differential scanning calorimetry (MDSC) in food and drug industries. *Polymers* 12, 5. doi:10.3390/polym12010005

Li, B., Ling, T.-C., Yu, J.-G., Wu, J., and Chen, W. (2019). Cement pastes modified with recycled glass and supplementary cementitious materials: properties at the ambient and high temperatures. *J. Clean. Prod.* 241, 118155. doi:10.1016/j.jclepro.2019.118155

Lisa, H., Pedro, M., Eiichi, O., Milos, T., and Hendrik, G. van O. (2006). 2006 IPCC guidelines for national greenhouse gas inventories, volume 3: industrial processes and product use, chapter 2: mineral industry emissions. *IPCC Natl. Greenh. Gas. Invent. Programme*. Available at: https://www.ipcc-nggip.iges.or.jp/public/2006gl/vol3.html.

Luo, F., Tang, H., Shu, X., Chen, S., Li, B., Shi, K., et al. (2021). Immobilization of uranium-contaminated soil into glass waste by microwave sintering: experimental and theoretical study. *J. Non-Cryst. Solids* 556, 120551. doi:10.1016/j.jnoncrysol.2020.120551

Ma, J., Chen, C. Z., Wang, D. G., and Hu, J. H. (2011). Synthesis, characterization and *in vitro* bioactivity of magnesium-doped sol–gel glass and glass-ceramics. *Ceram. Int.* 37, 1637–1644. doi:10.1016/j.ceramint.2011.01.043

Ma, M., Ni, W., Wang, Y., Wang, Z., and Liu, F. (2008). The effect of TiO2 on phase separation and crystallization of glass-ceramics in CaO–MgO–Al2O3–SiO2–Na2O system. *J. Non-Cryst. Solids* 354, 5395–5401. doi:10.1016/j.jnoncrysol.2008.09.019

Mackenzie, J. D. (1982). Glasses from melts and glasses from gels, a comparison. *J. Non-Cryst. Solids* 48, 1–10. doi:10.1016/0022-3093(82)90241-1

Mascaraque, N., Bauchy, M., and Smedskjaer, M. M. (2017). Correlating the network topology of oxide glasses with their chemical durability. *J. Phys. Chem. B* 121, 1139–1147. doi:10.1021/acs.jpcb.6b11371

Micoulaut, M., Bauchy, M., and Flores-Ruiz, H. (2015). "Topological constraints, rigidity transitions, and anomalies in molecular networks," in *Molecular dynamics simulations of disordered materials: from network glasses to phase-change memory alloys*. Editors C. Massobrio, J. Du, M. Bernasconi, and P. S. Salmon (Cham: Springer International Publishing), 275–311. doi:10.1007/978-3-319-15675-0_11

Minet, J., Abramson, S., Bresson, B., Franceschini, A., Damme, H. V., and Lequeux, N. (2006). Organic calcium silicate hydrate hybrids: a new approach to cement based nanocomposites. *J. Mat. Chem.* 16, 1379–1383. doi:10.1039/B515947D

Misbah, M. H., El-Kemary, M., and Ramadan, R. (2021). Effect of Mg2+ coordination on the structural and optical properties of iron magnesium phosphate glasses. *J. Non-Cryst. Solids* 569, 120987. doi:10.1016/j.jnoncrysol.2021.120987

Montazerian, M., Schneider, J. F., Yekta, B. E., Marghussian, V. K., Rodrigues, A. M., and Zanotto, E. D. (2015). Sol–gel synthesis, structure, sintering and properties of bioactive and inert nano-apatite–zirconia glass–ceramics. *Ceram. Int.* 41, 11024–11045. doi:10.1016/j.ceramint.2015.05.047

Mysen, B. O. (1987). Redox equilibria and coordination of Fe2+ and Fe3+ in silicate glasses from 57Fe mossbauer spectroscopy. *J. Non-Cryst. Solids* 95 (96), 247–254. doi:10.1016/S0022-3093(87)80117-5

Nair, P. A. K., Vasconcelos, W. L., Paine, K., and Calabria-Holley, J. (2021). A review on applications of sol-gel science in cement. *Constr. Build. Mat.* 291, 123065. doi:10.1016/j.conbuildmat.2021.123065

Naito, K., and Miura, A. (1993). Molecular design for nonpolymeric organic dye glasses with thermal stability: relations between thermodynamic parameters and amorphous properties. *J. Phys. Chem.* 97, 6240–6248. doi:10.1021/j100125a025

Nie, S., Thomsen, R. M., and Skibsted, J. (2020). Impact of Mg substitution on the structure and pozzolanic reactivity of calcium aluminosilicate (CaO-Al2O3-SiO2) glasses. *Cem. Concr. Res.* 138, 106231. doi:10.1016/j.cemconres.2020.106231

Nommeots-Nomm, A., Houaoui, A., Pradeepan Packiyanathar, A., Chen, X., Hokka, M., Hill, R., et al. (2020). Phosphate/oxyfluorophosphate glass crystallization and its impact on dissolution and cytotoxicity. *Mat. Sci. Eng. C* 117, 111269. doi:10.1016/j.msec.2020.111269

Oey, T., La Plante, E. C., Falzone, G., Yang, K., Wada, A., Bauchy, M., et al. (2020). Topological controls on aluminosilicate glass dissolution: complexities induced in hyperalkaline aqueous environments. *J. Am. Ceram. Soc.* 103, 6198–6207. doi:10.1111/jace.17357

Perez, A., Daval, D., Fournier, M., Vital, M., Delaye, J.-M., and Gin, S. (2019). Comparing the reactivity of glasses with their crystalline equivalents: the case study of plagioclase feldspar. *Geochim. Cosmochim. Acta* 254, 122–141. doi:10.1016/j.gca.2019.03.030

Peys, A., Isteri, V., Yliniemi, J., Yorkshire, A. S., Lemougna, P. N., Utton, C., et al. (2022). Sustainable iron-rich cements: raw material sources and binder types. *Cem. Concr. Res.* 157, 106834. doi:10.1016/j.cemconres.2022.106834

Pinakidou, F., Katsikini, M., Kavouras, P., Komninou, F., Karakostas, Th., and Paloura, E. C. (2008). Structural role and coordination environment of Fe in Fe2O3–PbO–SiO2–Na2O composite glasses. *J. Non-Cryst. Solids* 354, 105–111. doi:10.1016/j.jnoncrysol.2007.07.028

Pinakidou, F., Katsikini, M., Paloura, E. C., Kalogirou, O., and Erko, A. (2007). On the local coordination of Fe in Fe2O3-glass and Fe2O3-glass ceramic systems containing Pb, Na and Si. *J. Non-Cryst. Solids* 353, 2717–2733. doi:10.1016/j.jnoncrysol.2007.05.007

Rada, S., Dehelean, A., and Culea, E. (2011). FTIR, Raman, and UV-Vis spectroscopic and DFT investigations of the structure of iron–lead–tellurate glasses. *J. Mol. Model.* 17, 2103–2111. doi:10.1007/s00894-010-0911-5

Ren, H., Tian, Y., Li, A., Martin, R. A., and Qiu, D. (2017). The influence of phosphorus precursor on the structure and properties of SiO 2 –P 2 O 5 –CaO bioactive glass. *Biomed. Phys. Eng. Express* 3, 045017. doi:10.1088/2057-1976/aa7daa

Saravanapavan, P., and Hench, L. L. (2003). Mesoporous calcium silicate glasses. I. Synthesis. *J. Non-Cryst. Solids* 318, 1–13. doi:10.1016/S0022-3093(02)01864-1

Sawyer, R., Nesbitt, H. W., and Secco, R. A. (2012). High resolution X-ray Photoelectron Spectroscopy (XPS) study of K2O–SiO2 glasses: evidence for three types of O and at least two types of Si. *J. Non-Cryst. Solids* 358, 290–302. doi:10.1016/j.jnoncrysol.2011.09.027

Schöler, A., Winnefeld, F., Haha, M. B., and Lothenbach, B. (2017). The effect of glass composition on the reactivity of synthetic glasses. *J. Am. Ceram. Soc.* 100, 2553–2567. doi:10.1111/jace.14759

Scholtzová, E., Smrčok, L., Tunega, D., and Turi Nagy, L. (2000). *Ab initio* 2-D periodic Hartree–Fock study of Fe-substituted lizardite 1T– a simplified cronstedtite model. *Phys. Chem. Min.* 27, 741–746. doi:10.1007/s002690000107

Scrivener, K. L., John, V. M., and Gartner, E. M. (2018). Eco-efficient cements: potential economically viable solutions for a low-CO2 cement-based materials industry. *Cem. Concr. Res.* 114, 2–26. doi:10.1016/j.cemconres.2018.03.015

Senkov, O. N., Scott, J. M., and Miracle, D. B. (2002). Crystallization kinetics of an amorphous Al85Ni10Y2.5La2.5 alloy. *J. Alloys Compd.* 337, 83–88. doi:10.1016/S0925-8388(01)01909-0

Serdar, M., Bjegovic, D., Stirmer, N., and Banjad Pecur, I. (2019). "Alternative binders for concrete: opportunities and challenges," in *Future trends in civil engineering* (Zagreb, Croatia: University of Zagreb Faculty of Civil Engineering), 199–218. doi:10.5592/CO/FTCE.2019.09

Shankhwar, N., and Srinivasan, A. (2016). Evaluation of sol–gel based magnetic 45S5 bioglass and bioglass–ceramics containing iron oxide. *Mat. Sci. Eng. C* 62, 190–196. doi:10.1016/j.msec.2016.01.054

Shanks, B., Howe, C., Draper, S., Wong, H., and Cheeseman, C. (2024). Production of low-carbon amorphous SiO2 for use as a supplementary cementitious material and nesquehonite from olivine. *Mat. Lett.* 361, 136133. doi:10.1016/j.matlet.2024.136133

Sharma, P. U., Modi, K. B., Lakhani, V. K., Zankat, K. B., and Joshi, H. H. (2007). Mössbauer spectroscopic studies of Fe3+-substituted YIG. *Ceram. Int.* 33, 1543–1546. doi:10.1016/j.ceramint.2006.06.012

Simonsen, M. E., Sønderby, C., Li, Z., and Søgaard, E. G. (2009). XPS and FT-IR investigation of silicate polymers. *J. Mat. Sci.* 44, 2079–2088. doi:10.1007/s10853-009-3270-9

Skibsted, J., and Snellings, R. (2019a). Reactivity of supplementary cementitious materials (SCMs) in cement blends. *Cem. Concr. Res.* 124, 105799. doi:10.1016/j.cemconres.2019.105799

Skibsted, J., and Snellings, R. (2019b). Reactivity of supplementary cementitious materials (SCMs) in cement blends. *Cem. Concr. Res.* 124, 105799. doi:10.1016/j.cemconres.2019.105799

Snellings, R. (2013). Solution-controlled dissolution of supplementary cementitious material glasses at pH 13: the effect of solution composition on glass dissolution rates. *J. Am. Ceram. Soc.* 96, 2467–2475. doi:10.1111/jace.12480

Snellings, R., Suraneni, P., and Skibsted, J. (2023). Future and emerging supplementary cementitious materials. *Cem. Concr. Res.* 171, 107199. doi:10.1016/j.cemconres.2023.107199

Stone-Weiss, N., Youngman, R. E., Thorpe, R., Smith, N. J., Pierce, E. M., and Goel, A. (2020). An insight into the corrosion of alkali aluminoborosilicate glasses in acidic environments. *Phys. Chem. Chem. Phys.* 22, 1881–1896. doi:10.1039/C9CP06064B

Van De Leest, R. E., and Roozeboom, F. (1998). Iron-silicate glassy films by sol-gel conversion induced by rapid thermal processing. *MRS Online Proc. Libr.* 525, 351–358. doi:10.1557/PROC-525-351

Walker, L. R., Wertheim, G. K., and Jaccarino, V. (1961). Interpretation of the Fe57 Isomer Shift. *Phys. Rev. Lett.* 6, 98–101. doi:10.1103/PhysRevLett.6.98

Weisinger, J. R., and Bellorín-Font, E. (1998). Magnesium and phosphorus. *Lancet* 352, 391–396. doi:10.1016/S0140-6736(97)10535-9

Wenzel, J. (1985). Trends in sol—gel processing: toward 2004. *J. Non-Cryst. Solids* 73, 693–699. doi:10.1016/0022-3093(85)90389-8

Xu, X., Bertani, M., Saini, R., Kamali, S., Neuville, D. R., Youngman, R. E., et al. (2024). Iron-induced structural rearrangements and their impact on sulfur solubility in borosilicate-based nuclear waste glasses. *J. Phys. Chem. C* 128, 11870–11887. doi:10.1021/acs.jpcc.4c02085

Yliniemi, J. (2022). Surface layer alteration of multi-oxide silicate glasses at a near-neutral pH in the presence of citric and tartaric acid. *Langmuir* 38, 987–1000. doi:10.1021/acs.langmuir.1c02378

Yoldas, B. E. (1982). Introduction and effect of structural variations in inorganic polymers and glass networks. *J. Non-Cryst. Solids* 51, 105–121. doi:10.1016/0022-3093(82)90191-0

Yoshio, T., Kawaguchi, C., Kanamaru, F., and Takahashi, K. (1981). Characterization of alkoxy-derived iron silicate. *J. Non-Cryst. Solids* 43, 129–140. doi:10.1016/0022-3093(81)90179-4

Zarzuela, R., Luna, M., Carrascosa, L. M., Yeste, M. P., Garcia-Lodeiro, I., Blanco-Varela, M. T., et al. (2020). Producing C-S-H gel by reaction between silica oligomers and portlandite: a promising approach to repair cementitious materials. *Cem. Concr. Res.* 130, 106008. doi:10.1016/j.cemconres.2020.106008

Zhao, Z., Song, Y., Min, X., Liang, Y., Chai, L., and Shi, M. (2016). XPS and FTIR studies of sodium arsenate vitrification by cullet. *J. Non-Cryst. Solids* 452, 238–244. doi:10.1016/j.jnoncrysol.2016.08.028

Zheng, K., and Boccaccini, A. R. (2017). Sol-gel processing of bioactive glass nanoparticles: a review. *Adv. Colloid Interface Sci.* 249, 363–373. doi:10.1016/j.cis.2017.03.008